Cell Reports

Article

# A presynaptic phosphosignaling hub for lasting homeostatic plasticity

## Graphical abstract

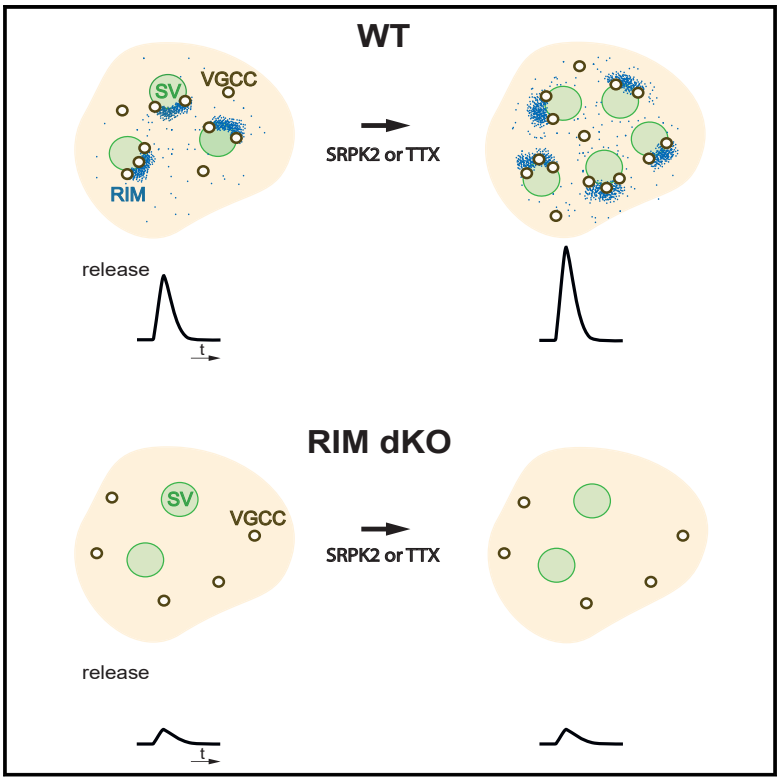


## Authors

Johannes Alexander Müller, Julia Betzin, Jorge Santos-Tejedor, ..., Mark E. Graham, Dirk Dietrich, Susanne Schoch

## Correspondence

dirk.dietrich@uni-bonn.de (D.D.), susanne.schoch@uni-bonn.de (S.S.)

## In brief

The amount of neurotransmitters released in response to an action potential can be tuned by altering the number of release sites. Müller et al. show that the kinase SRPK2 is involved in regulating this process via the presynaptic active-zone protein RIM. Phosphorylation status changes of RIM dynamically modulate synaptic strength.

## Highlights

- RIM is required for induction of presynaptic homeostatic plasticity (PHP)
- The kinase SRPK2 regulates basal synaptic vesicle release and PHP
- SRPK2 controls the number of RIM nanoclusters and of docked synaptic vesicles
- Phosphorylation of RIM1 at serine 1045 increases release and occludes PHP

Müller et al., 2022, Cell Reports *39*, 110696
April 19, 2022 
https://doi.org/10.1016/j.celrep.2022.110696

CellPress

Cell Reports

CellPress
OPEN ACCESS

Article

# A presynaptic phosphosignaling hub for lasting homeostatic plasticity

Johannes Alexander Müller,[1,2,9] Julia Betzin,[1,9] Jorge Santos-Tejedor,[1] Annika Mayer,[1] Ana-Maria Oprişoreanu,[1,8] Kasper Engholm-Keller,[3,4] Isabelle Paulußen,[2] Polina Gulakova,[1,2] Terrence Daniel McGovern,[2] Lena Johanna Gschossman,[1,2] Eva Schönhense,[1] Jesse R. Wark,[4] Alf Lamprecht,[5] Albert J. Becker,[1] Ashley J. Waardenberg,[6,7] Mark E. Graham,[4] Dirk Dietrich,[2,10,*] and Susanne Schoch[1,10,11,*]

[1]Section for Translational Epilepsy Research, Department of Neuropathology, University Hospital Bonn, Bonn, Germany
[2]Department of Neurosurgery, University Hospital Bonn, Bonn, Germany
[3]Department of Biochemistry and Molecular Biology, University of Southern Denmark, Odense, Denmark
[4]Synapse Proteomics, Children's Medical Research Institute, The University of Sydney, Westmead, NSW, Australia
[5]Department of Pharmaceutics, Bonn University, Bonn, Germany
[6]Australian Institute for Tropical Health and Medicine, James Cook University, Smithfield, QLD 4878, Australia
[7]i-Synapse, Cairns, QLD, Australia
[8]Present address: Center for Regenerative Therapies Dresden, Technical University Dresden, Dresden, Germany
[9]These authors contributed equally
[10]These authors contributed equally
[11]Lead contact
*Correspondence: dirk.dietrich@uni-bonn.de (D.D.), susanne.schoch@uni-bonn.de (S.S.)
https://doi.org/10.1016/j.celrep.2022.110696

## SUMMARY

Stable function of networks requires that synapses adapt their strength to levels of neuronal activity, and failure to do so results in cognitive disorders. How such homeostatic regulation may be implemented in mammalian synapses remains poorly understood. Here we show that the phosphorylation status of several positions of the active-zone (AZ) protein RIM1 are relevant for synaptic glutamate release. Position RIMS1045 is necessary and sufficient for expression of silencing-induced homeostatic plasticity and is kept phosphorylated by serine arginine protein kinase 2 (SRPK2). SRPK2-induced upscaling of synaptic release leads to additional RIM1 nanoclusters and docked vesicles at the AZ and is not observed in the absence of RIM1 and occluded by RIM$^{S1045E}$. Our data suggest that SRPK2 and RIM1 represent a presynaptic phosphosignaling hub that is involved in the homeostatic balance of synaptic coupling of neuronal networks.

## INTRODUCTION

Synapses, the major sites of neuron-to-neuron communication, act not only as relay stations by rapidly releasing neurotransmitters with tight temporal and spatial control but also contribute to storage, transmission, and recall of information by acute synaptic computation and activity-dependent strengthening and weakening of individual synapses (Buzsáki, 2010; Poo et al., 2016). Presynaptic homeostatic plasticity (PHP), the ability of neurons to scale their synaptic output to changes in activity, is a major mechanism by which neurons maintain synaptic transmission in the physiological range in response to perturbations of neuronal network activity (Marder and Prinz, 2002; Miller, 1996; Turrigiano and Nelson, 2004). PHP, as opposed to coexisting postsynaptic mechanisms of homeostatic plasticity (HP) regulating synaptic strength, strongly modifies the temporal transmission properties at individual synapses because the level of transmitter release and short-term synaptic plasticity are tightly linked (Delvendahl and Müller, 2019). Although a neuron broadcasts the same pattern of action potential activity to all of its presynapses, it is the function of PHP to enable the presynaptic neuron to adjust the resulting temporal pattern of vesicle release at each synapse to match the requirements of the postsynaptic partner.

PHP has been identified in various organisms, at different central nervous system (CNS) synapse types (Frank et al., 2020; Delvendahl and Müller, 2019), and is recruited *in vivo* (Cull-Candy et al., 1980; Zhuang et al., 2020). There is increasing evidence linking PHP to neurological diseases like schizophrenia, autism, epilepsy, and degenerative disorders (Lignani et al., 2020; Orr et al., 2020; Genç et al., 2020). Still, our knowledge about how the function of individual proteins is modified and how this contributes to the persistent alterations in vesicle release during PHP in mammalian synapses is very limited.

At hippocampal synapses, the increased synaptic strength observed during PHP has been shown to correlate to changes in the size of the presynaptic active zone (AZ), the number of docked synaptic vesicles (SVs) (Murthy et al., 2001), improved transsynaptic alignment of nanoclusters (Chen et al., 2018), and the abundance of AZ components (Lazarevic et al., 2011; Schanzenbächer et al., 2016). However, it is still unresolved what the triggers of those changes are and how they are maintained to achieve persistent potentiation of synaptic strength and effective PHP.

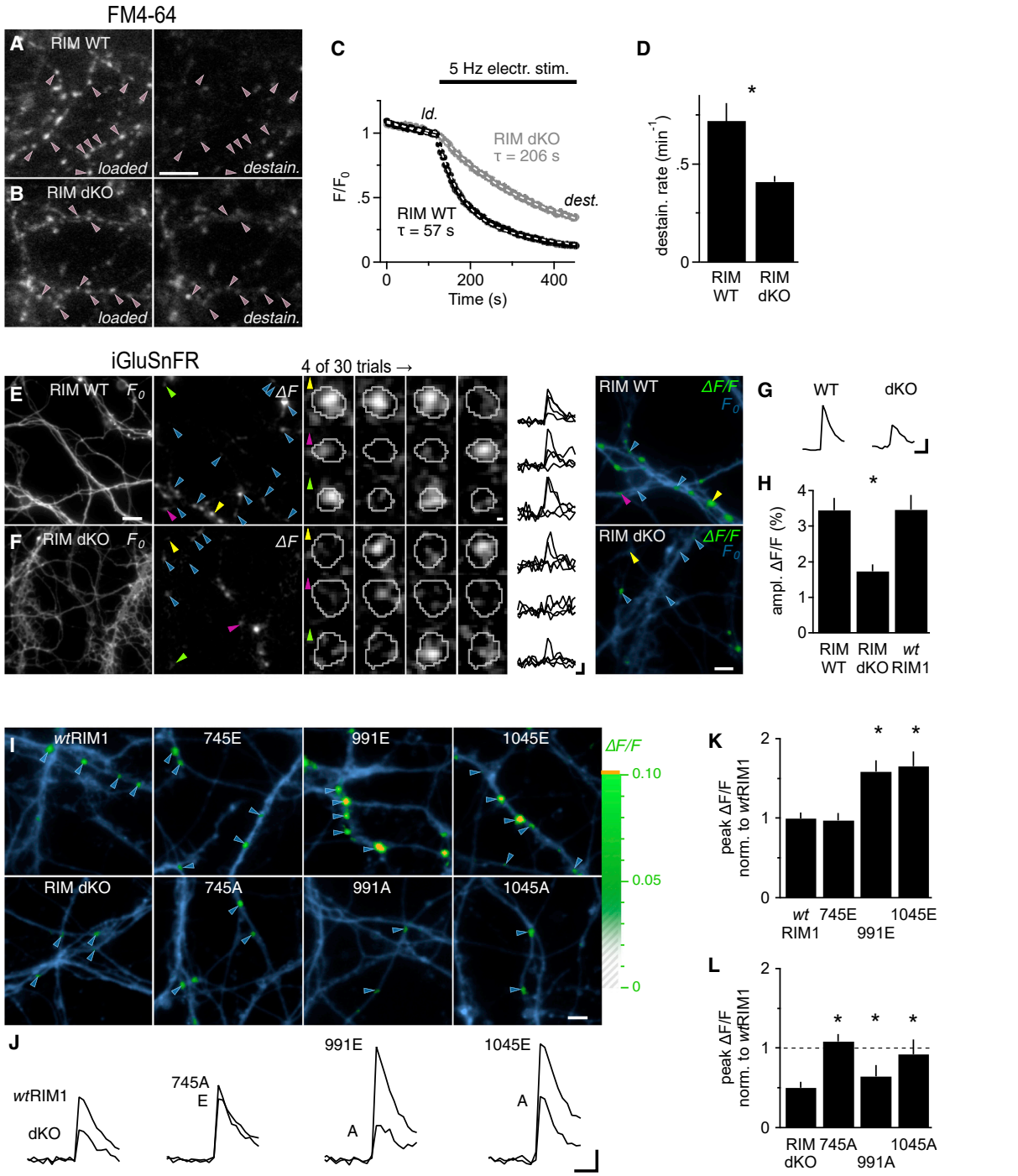


**Figure 1. Phosphorylation of S991 and S1045 in RIM1 potentiates glutamate release**

(A and B) Representative images of RIM1/2 WT (A, RIM WT, 15 DIV) and double knockout (B, RIM dKO) neurons after loading SVs with the fluorescent dye FM4-64 (left, loaded) and after 5-Hz electrical field potential stimulation (right, destain.). Arrowheads indicate synaptic structures that were used for analysis. Scale bar, 10 μm.

(C and D) Average destaining rates of experiments shown in (A) and (B) (black, RIM WT; gray, RIM dKO). Dashed white lines represent exponential-like fits (see STAR Methods for details). Time points shown in (A) and (B) are indicated by loaded (ld) and destain (dest). n = 8 experiments for RIM WT and RIM dKO each, unpaired t test.

(E and F) Representative fluorescence wide-field images showing iGluSnFR expression ($F_0$, left panel) in RIM WT (E) and RIM dKO (F) neurons. Images of the ΔF signal of the same field of view show sites of glutamate release (second panel from the left; scale bar, 10 μm). Arrowheads indicate analyzed regions of interest (ROIs). Small images show 4 of 30 trials for three selected ROIs (yellow, magenta, and green arrowheads; scale bar, 0.5 μm). ΔF/F signal traces of the three selected ROIs for the four illustrated trials are displayed on the right. Scale bars: 50 ms, 5%. Rightmost images show higher magnifications of iGluSnFR expression (blue) and superimposed average ΔF/F signals (green; scale bar, 5 μm). Analyzed release sites are indicated by arrowheads and color-coded as before.

*(legend continued on next page)*

This lack of knowledge about the major signaling hubs controlling PHP at mammalian CNS synapses is due to the fact that this form of plasticity has mainly been studied at the larval neuromuscular junction (NMJ) of *Drosophila* (Delvendahl and Müller, 2019), a synapse type that differs in its properties substantially from CNS synapses. First, NMJ synapses are not integrated in a neuronal network (terminal points); second, PHP is induced postsynaptically by acutely blocking glutamate receptors with philanthotoxin or chronically by their removal/knockout (Davis and Müller, 2015; Frank et al., 2020). In contrast, at CNS synapses, PHP can be triggered by chronic silencing of neurons, suggesting that different signaling pathways might be recruited (Turrigiano et al., 1998). In this non-mammalian system, genetic screens and loss-of-function mutants have uncovered around 15 genes, ranging from cell adhesion molecules to AZ components and channels, that are required for expression of PHP (Frank et al., 2020). Although a signaling pathway regulating these proteins during PHP has not yet been identified, one of the proteins that has been found to be essential for PHP at the *Drosophila* NMJ (Müller et al., 2012) and for presynaptically mediated forms of long-term potentiation at CNS synapses (Castillo et al., 2002; Fourcaudot et al., 2008; Pelkey et al., 2008) is the central AZ component Rab3-interacting molecule 1 (RIM1).

RIM1 is necessary for docking and priming of SVs and anchors voltage-gated calcium channels at the AZ (Deng et al., 2011; Han et al., 2011; Kaeser et al., 2011; Schoch et al., 2002, 2006); therefore, it seems to be ideally suited to regulate vesicle release. However, with regard to presynaptic plasticity, it is still unclear how (1) RIM1's function in the synapse can be enhanced or weakened and (2) how an altered function of RIM1 can be made durable so that changes in release outlast the induction trigger for hours or even days. Phosphorylation of serine 413 has been suggested to underlie RIM1's role in presynaptic plasticity, but a phospho-deficient knockin mouse did not validate the *in vitro* data (Kaeser et al., 2008; Lonart et al., 2003). Therefore, even though RIM1 has been shown to be extensively and dynamically phosphorylated in response to activity (Desch et al., 2021; Engholm-Keller et al., 2019; Kohansal-Nodehi et al., 2016), the functional relevance of the phosphorylation sites and the operating kinases have not yet been identified.

## RESULTS

### Phospho-mimic mutations at serine 991 and 1,045 in RIM1 potentiate release

To precisely study the role of the AZ proteins RIM1/2 in regulating transmitter release, excluding synapse and culture density as well as stimulation strength as potential confounding factors, we only conducted functional analyses at the level of individual synapses. We infected cultured hippocampal neurons prepared from RIM1/2 double-floxed mice (RIM1/2$^{lox/lox}$) with lentiviruses expressing active or inactive mutant Cre recombinase to yield RIM double knockout (dKO) and RIM wild-type (WT) cells. We quantified the reduction in transmitter release resulting from RIM1/2 deletion using the styryl dye FM4-64 (Figures 1A–1D) and the glutamate sensor iGluSnFR (Marvin et al., 2013; Figures 1E–1H) in live-cell imaging experiments. Deletion of RIM1/2 significantly reduced the FM4-64 destaining rate to ~57% (0.72 ± 0.09, 0.41 ± 0.03 evoked destaining rates [min$^{-1}$] in RIM WT and RIM dKO, respectively; Figures 1A–1D, STAR Methods; Figures S1A–S1C), suggesting that the amount of SV release per action potential drops by ~40% in the absence of RIM1/2.

The glutamate sensor iGluSnFR.V184A was expressed in RIM dKO and RIM WT hippocampal neurons (Figures 1E–1H; Figures S1D–S1G; Marvin et al., 2018). Single weak electrical stimulations (STAR Methods) generated rapidly rising, very local fluorescent transients along neurites (Figures 1E and 1F). These fluorescent signals showed a substantial trial-to-trial variation in amplitude as well as a frequent failure to stimulation (Figures 1E–1F; Figures S1F, S1G, and S2A). Overall, their kinetics were reproducible (Figures S2A and S2C) and predominantly occurred at the same position (Figures 1E and 1F), in a manner sensitive to tetrodotoxin (TTX) (Figure S2B). Thus, we interpreted iGluSnFR transients in response to weak stimulation as optical correlates of action potential-induced quantal glutamate release (Dürst et al., 2019). We assessed the mean transmitter release per synapse by averaging subsequently recorded trials of stimulation. In the resulting average frame series, we identified several regions of interest (STAR Methods; Figures 1E and 1F; Figures S1D–S1G) containing individual synapses and quantified transmitter release as the peak amplitude of the ΔF/F signal. We found release in individual glutamatergic synapses to be significantly reduced to ~51% by deletion of RIM1/2 (ΔF/F amplitudes: RIM WT, 3.45% ± 0.34%; RIM dKO, 1.73% ± 0.19%; Figures 1G and 1H). This reduction in release was fully restored by co-transducing WT full-length RIM1 (*wt*RIM1) in the Cre-induced RIM1/2 dKO neurons (ΔF/F amplitude [percent]: 3.46% ± 0.41%; Figure 1H and Figure S3).

To test the functional relevance of individual phosphorylation sites in RIM1, they were mutated to a phospho-deficient (S to A) or phospho-mimic (S to E) variant. These phospho-mutant RIM1 variants were expressed in RIM dKO hippocampal neurons and subjected to iGluSnFR-based analysis of glutamate release at individual synapses. For some phosphorylation sites (for example S745 of RIM1), the phosphorylation status had no effect

(G) Average ΔF/F traces from experiments shown in (E) and (F). Scale bars, 100 ms, 1%.
(H) Average ΔF/F iGluSnFR signal peak amplitudes of RIM WT, RIM dKO, and RIM dKO neurons transduced with *wt*RIM1. n = 12, 10, and 6 experiments for RIM WT, RIM dKO, and *wt*RIM1, respectively. One-way ANOVA with Holm-Sidak post hoc test for 2 comparisons (ANOVA-HS 2 comp.) against RIM WT.
(I) iGluSnFR expression in RIM dKO neurons (without recombinant RIM or transduced with the indicated RIM1 variants) with superimposed average ΔF/F iGluSnFR responses. Blue arrowheads point to analyzed release sites. Scale bar, 5 μm.
(J) Average ΔF/F iGluSnFR traces of the experiments shown in (I). Scale bars, 100 ms, 1%.
(K) Average iGluSnFR signal amplitudes. n = 18, 11, 23, and 17 experiments for *wt*RIM1, RIM1$^{S745E}$, RIM1$^{S991E}$, and RIM1$^{S1045E}$, respectively; ANOVA-HS 3 comp. against *wt*RIM1.
(L) Average iGluSnFR signal amplitudes (the dashed line indicates *wt*RIM1 levels as shown in K). n = 10, 9, 8, and 12 experiments for RIM dKO, RIM1$^{S745A}$, RIM1$^{S991A}$, and RIM1$^{S1045A}$, respectively; ANOVA-HS 3 comp. against RIM dKO. (D), (H), (K), (L) Data are shown as mean ± SEM and differences were considered statistically significant if $p < 0.05$.

on transmitter release because S745A and E restored release to levels measured when *wt*RIM1 was expressed in dKO neurons (peak ΔF/F norm. to *wt*RIM1: $RIM1^{S745E}$, 0.97 ± 0.09; $RIM1^{S745A}$, 1.08 ± 0.13; Figures 1I–1L). In contrast, we identified two sites, S991 and S1045, whose phosphorylation status affected basal synaptic transmitter release (Figures 1I–1L). $RIM1^{S991E}$ and $RIM1^{S1045E}$ substantially and significantly potentiated release by ~60% compared with *wt*RIM1 (peak ΔF/F norm. to *wt*RIM1: $RIM1^{S991E}$, 1.59 ± 0.14; $RIM1^{S1045E}$, 1.65 ± 0.19; Figures 1J and 1K). Although $RIM1^{S1045A}$ behaved as *wt*RIM1 and significantly increased release compared with RIM dKO (peak ΔF/F norm. to *wt*RIM1: 0.92 ± 0.05; Figures 1J and 1L), $RIM1^{S991A}$ only slightly increased release above RIM dKO levels (peak ΔF/F norm. to *wt*RIM1: 0.65 ± 0.05; Figures 1J and 1L). Immunocytochemistry showed that $RIM1^{S991A}$ is efficiently transported to presynaptic sites and detected there at levels similar to *wt*RIM1, $RIM1^{S745A}$, and $RIM1^{S1045A}$ (Figure S3). These data suggest that endogenous RIM1 under basal conditions may not be phosphorylated at site S1045, whereas a mixed phosphorylation status may exist at site S991 (~50/50) and that both sites could mediate an increase in release upon complete phosphorylation through a presynaptic kinase.

## Silencing-induced PHP requires RIM1 and increases the number of RIM1 nanoclusters in the AZ

Silencing cultured neurons with 1 μM TTX for 48 h (Turrigiano et al., 1998) led to a pronounced and significant, ~70% increase in iGluSnFR responses after washout of TTX for 10 min (1.68 ± 0.21-fold increase in the peak of average ΔF/F signal; Figures 2A, 2B, and 2E). This potentiation was RIM1/2 dependent because treating RIM dKO neurons with TTX did not increase transmitter output (0.90 ± 0.08-fold increase in the peak of average ΔF/F signal; Figures 2C–2E). This indicates that RIM1/2 is essential for silencing-induced HP.

RIM1/2 form nanoclusters at the presynaptic AZ that mark sites of SV release (Tang et al., 2016). We therefore wanted to determine whether the observed RIM-dependent silencing-induced increase in synaptic release is accompanied by an increase in RIM1/2 nanoclusters. To address this, we employed direct stochastic optical reconstruction microscopy (dSTORM) and counted the RIM1 nanoclusters in synapses identified by anti-synapsin staining in silenced (TTX, 48 h) versus control neurons (Figure 2F–2K; Figure S4). dSTORM imaging of fixed neurons revealed a significant, ~40% increase in the number of synaptic RIM1 nanoclusters (2.44 ± 0.15 and 3.46 ± 0.39 RIM1 nanoclusters per synapse in the control and post-silencing condition, respectively; Figures 2F–2H). Other parameters, like the number of RIM1 localizations per synapse, the RIM1 cluster density, and the area of RIM1 nanoclusters, were not significantly changed by TTX-induced silencing (Figures 2I–2K).

## RIM1 is the major binding partner of the kinase SRPK2 at the AZ

To identify potential RIM effectors involved in phosphorylation of RIM1, we searched for phospho-dependent RIM1 binding partners. We incubated the N-terminal (N-$t_{1–715}$; amino acids [aa] 1–715) and C-terminal (C-$t_{735-1615}$; aa 735–1615) half of RIM1 purified from HEK293T cells using a FLAG tag with lysed mouse crude synaptosomes in the presence of the kinase inhibitor staurosporine (1 μM), the phosphatase inhibitor phosSTOP (1×), or vehicle (control), followed by affinity purification, SDS-PAGE, and liquid chromatography-tandem mass spectrometry (LC-MS/MS) (Figures 3A and 3B). We obtained 39 (N-$t_{1–715}$) and 52 (C-$t_{735–1615}$) proteins that were discovered in at least two conditions, and for eight of these, their abundance seemed to co-vary with application of staurosporine or phosSTOP (Figure 3C). Only SRPK2 and PPP3CB demonstrated reduced immunoprecipitation after blocking kinase activity and bound more strongly in the presence of the phosphatase blocker (Figure 3C). Immunocytochemistry of mature hippocampal neurons revealed that SRPK2 is not only detected in the soma but also present in axons and dendrites (Figures S5A and S5B). We verified that SRPK2 binds to the RIM1 C2A and C2B domains using multiple methods, like co-immunoprecipitation (Figure S5C), an in-cell membrane-targeting assay based on Gap43-GFP-SRPK2 (Figure S5D), and two-photon fluorescence lifetime imaging microscopy (FLIM)-based fluorescence resonant energy transfer (FRET) experiments (Figures S5E–S5G). We tested whether SRPK2 directly interacts with additional components of the AZ by co-immunoprecipitation (Figure S5H) and found that, of five AZ proteins analyzed, only RIM1 and, to a lesser extent, ELKS1/2 bound to SRPK2. Binding to a kinase-dead variant of SRPK2 was reduced for both proteins (Figure S5I). Subcellular fractionation of the synaptic membrane followed by extraction with TX-100 revealed SRPK2 to be an integral component of the AZ (Figure S5J).

## SRPK2 regulates release in a RIM1-dependent manner

Next we probed whether the phosphorylation activity of SRPK2 affects synaptic transmission. To this end, we generated rAAV viral vectors for knockdown (KD; shSK2) and overexpression (OE; SK2) of the kinase and verified their efficiency in cultured hippocampal (Figures S6A and S6B) and cortical (Figures S6D and S6E) neurons. The ability of our viral constructs to modulate SRPK2 levels in synapses was confirmed by synaptosomes prepared from primary cortical neurons (Figure S6C).

To test the functional relevance of SRPK2, we compared the synaptic release efficacy of cultured neurons transduced with GFP (control [Ctr]), SRPK2, or shRNA-SRPK2 expressing rAAV viral particles. FM4-64 destaining rates of cultures (Figures 3D–3F) with experimentally elevated or lowered SRPK2 levels were significantly increased or decreased, respectively (0.66 ± 0.04, 0.88 ± 0.07, 0.55 ± 0.03 evoked destaining rates ($min^{-1}$) in Ctr, SK2 and shSK2, respectively, Figure 3F). Destaining rates in the absence of stimulation were not changed between conditions (Figure S6F).

These results were confirmed by iGluSnFR imaging experiments in which SRPK2 OE significantly increased transmitter output by ~42% compared with Ctr (to 142% ± 15% peak ΔF/F norm. to cells not expressing SRPK2; Figures 3G–3I). This potentiating effect likely involved phosphorylation because the kinase-dead version of SRPK2 did not increase release (73% ± 7% peak ΔF/F norm. to Ctr cells not expressing SKDead; Figures 3H and 3I). Quantitative immunocytochemistry of several AZ proteins after SRPK2 OE or KD revealed a selective increase in synaptic RIM1 levels under the OE condition (Figures S7A–S7E).

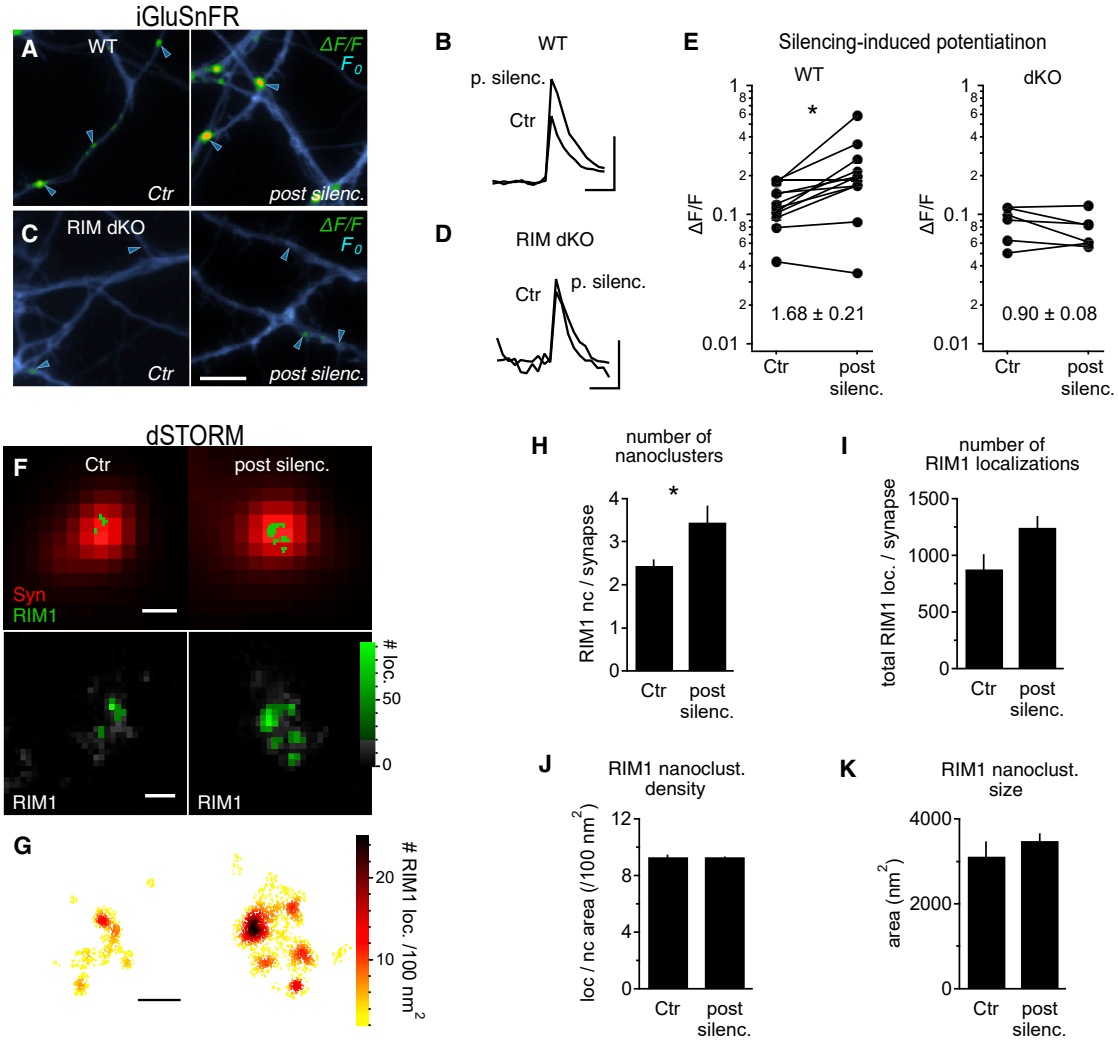


**Figure 2. PHP requires RIM1 and is associated with an increase in the number of RIM1 nanoclusters**

(A and C) iGluSnFR expression (blue, $F_0$) and superimposed ΔF/F (green) (color scale for ΔF/F as in Figure 1 and throughout the manuscript). Scale bar, 10 μm.

(B and D) Mean iGluSnFR ΔF/F traces from experiments shown in (A) and (C). Scale bars: 100 ms, 10%, and 100 ms, 5% for (B) and (D), respectively.

(E) ΔF/F peak amplitudes of paired experiments. Numbers in the lower half denote the mean ± SEM of the individual post-silencing/Ctr ratios (n = 12 and 7 experiments for WT and RIM dKO, respectively; paired ratio t test).

(F) dSTORM-based identification of RIM1 nanoclusters (green) superimposed on wide-field images of presynaptic boutons defined by Synapsin I (red, top row). Bottom row: Density histogram of RIM1 localizations). Scale bars, 200 nm (top) and 100 nm (bottom).

(G) Local density maps (r = 15 nm) of the RIM1 localizations shown in (F). Scale bar, 100 nm.

(H–K) Quantitative analysis of the number of RIM1 localizations and nanoclusters per presynaptic bouton (N = 6 cultures and n = 217 and 192 synapses for Ctr and post silenc., respectively; significance was tested across cultures; paired ratio t test). (H), (I), (J), (K) Data are shown as mean ± SEM and differences were considered statistically significant if $p < 0.05$.

Our data suggest that SRPK2 enhances synaptic transmission via regulation of RIM1. If that were the case, then SRPK2 should not potentiate release in the absence of RIM1/2. Although SRPK2 OE in WT neurons caused an ~1.5-fold increase in release compared with Ctr neurons (Figures 3I and 3L), the expression of SRPK2 in RIM dKO neurons did not significantly increase synaptic glutamate release compared with dKO neurons, as revealed by iGluSnFR imaging experiments (50.2% ± 5.4% and 48.5% ± 3.3% peak ΔF/F for RIM dKO and RIM dKO + SRPK2, respectively; norm. to the mean ΔF/F signal of RIM WT neurons; Figures 3J–3L). Our experiments suggest that SRPK2 increases basal synaptic release by regulating synaptic RIM1 levels.

## SRPK2 is required for and occludes HP

Next we wanted to determine whether SRPK2 may be a key player in HP. iGluSnFR imaging experiments after 48 h of TTX treatment showed that the silencing-induced upregulation of presynaptic release is blocked when SRPK2 levels were increased (1.10 ± 0.13-fold increase in signal amplitude

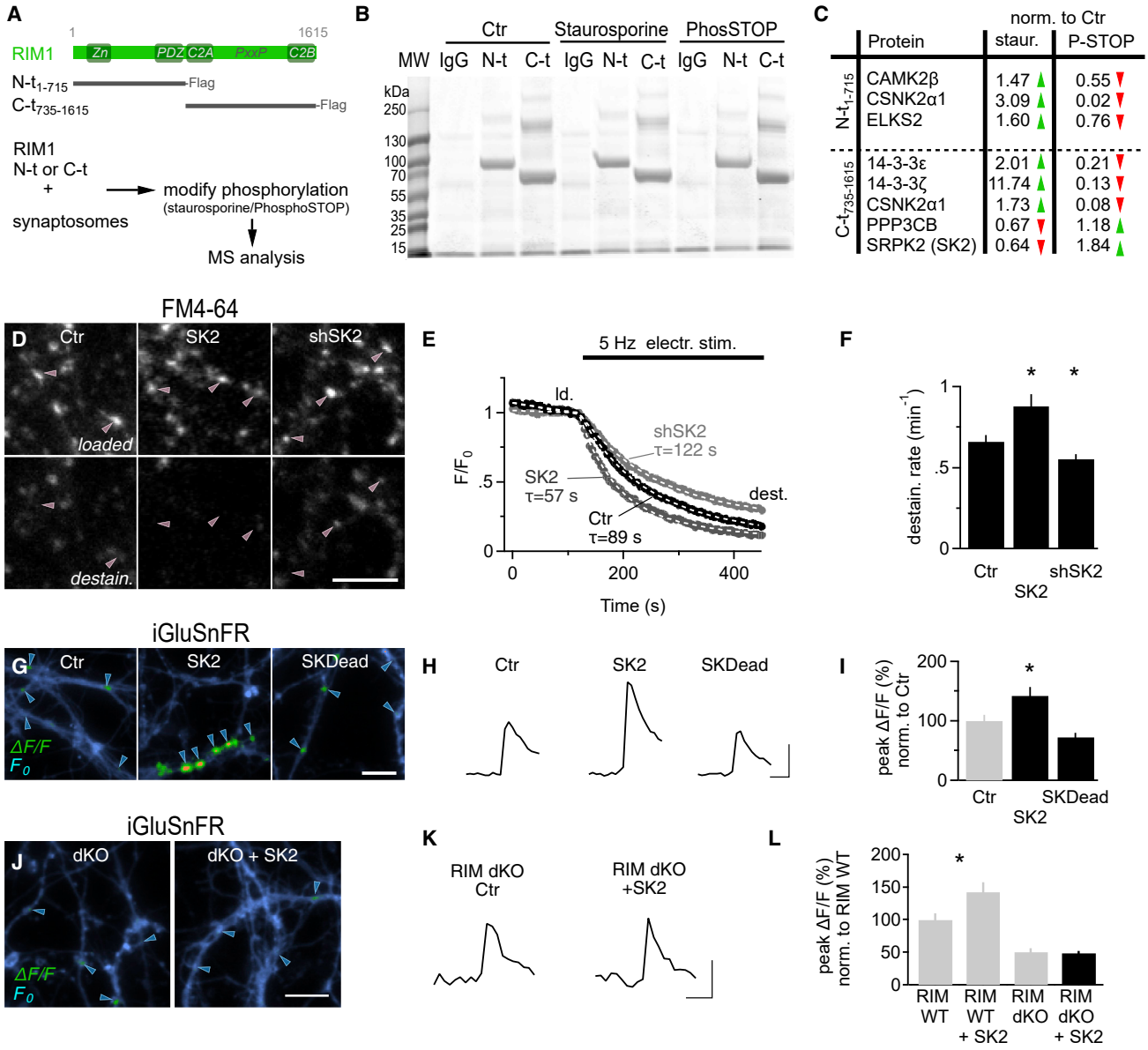


**Figure 3. SRPK2 interacts with RIM1, and its kinase activity regulates glutamate release**

(A) RIM1 fragments used to identify phospho-dependent RIM1 binding partners. MS, mass spectrometry.

(B) Coomassie blue-stained SDS-PAGE of immunoprecipitations of FLAG-tagged RIM1$^{1-715}$ (N-t), RIM1$^{735-1615}$ (C-t), and Ctr (immunoglobulin G [IgG]). MW, molecular weight.

(C) RIM1-interacting proteins identified by MS show decreased (red arrowheads) or increased (green arrowheads) binding under the staurosporine (staur) and PhosSTOP (P-STOP) condition compared with Ctr (values indicate fold change compared with Ctr; N-t$_{1-715}$, n = 2; C-t$_{735-1615}$, n = 4; n, independent replicates).

(D) Representative wide-field images of WT hippocampal neurons transduced with GFP (Ctr), SRPK2-GFP (SK2), or shSPRK2-GFP (shSK2) after loading SVs with FM4-64 (top row) and after destaining in response to 5-Hz field stimulation (bottom row). Pink arrowheads indicate analyzed synaptic structures. Scale bar, 10 μm.

(E and F) Average destaining rates of experiments shown in (D). Black, Ctr; dark gray, SK2; light gray, shSK2. Dashed white lines show the fits of the exponential decay function (see STAR Methods for details regarding fitting procedure). n = 9 experiments for each condition, ANOVA-HS 2 comp. against Ctr condition.

(G) iGluSnFR expression by WT hippocampal neurons with superimposed mean peak ΔF/F responses. Scale bar, 10 μm.

(H) Average iGluSnFR ΔF/F traces from experiments shown in (G). Scale bar, 100 ms, 2%.

(I) Average of iGluSnFR amplitudes. The gray bar (Ctr, RIM WT) represents reproduced (normalized) data from Figure 1H (n = 10 and 4 experiments for SK2 and SKDead, respectively; ANOVA-HS 2 comp. against Ctr).

(J) Mean ΔF/F peak responses of iGluSnFR superimposed on iGluSnFR expression (blue). Scale bar, 10 μm.

(K) Average iGluSnFR ΔF/F traces from the experiments shown in (J). Scale bar, 100 ms, 1%.

(L) Summary of iGluSnFR amplitudes. Gray bars are reproduced from (I) and Figure 1L to illustrate that, in contrast to WT neurons, SRPK2 OE does not significantly increase glutamate release in RIM dKO neurons (n = 10 and 6 experiments for RIM dKO and RIM dKO + SK2, respectively; unpaired t test). (F), (I), (L) Data are shown as mean ± SEM and differences were considered statistically significant if $p < 0.05$.

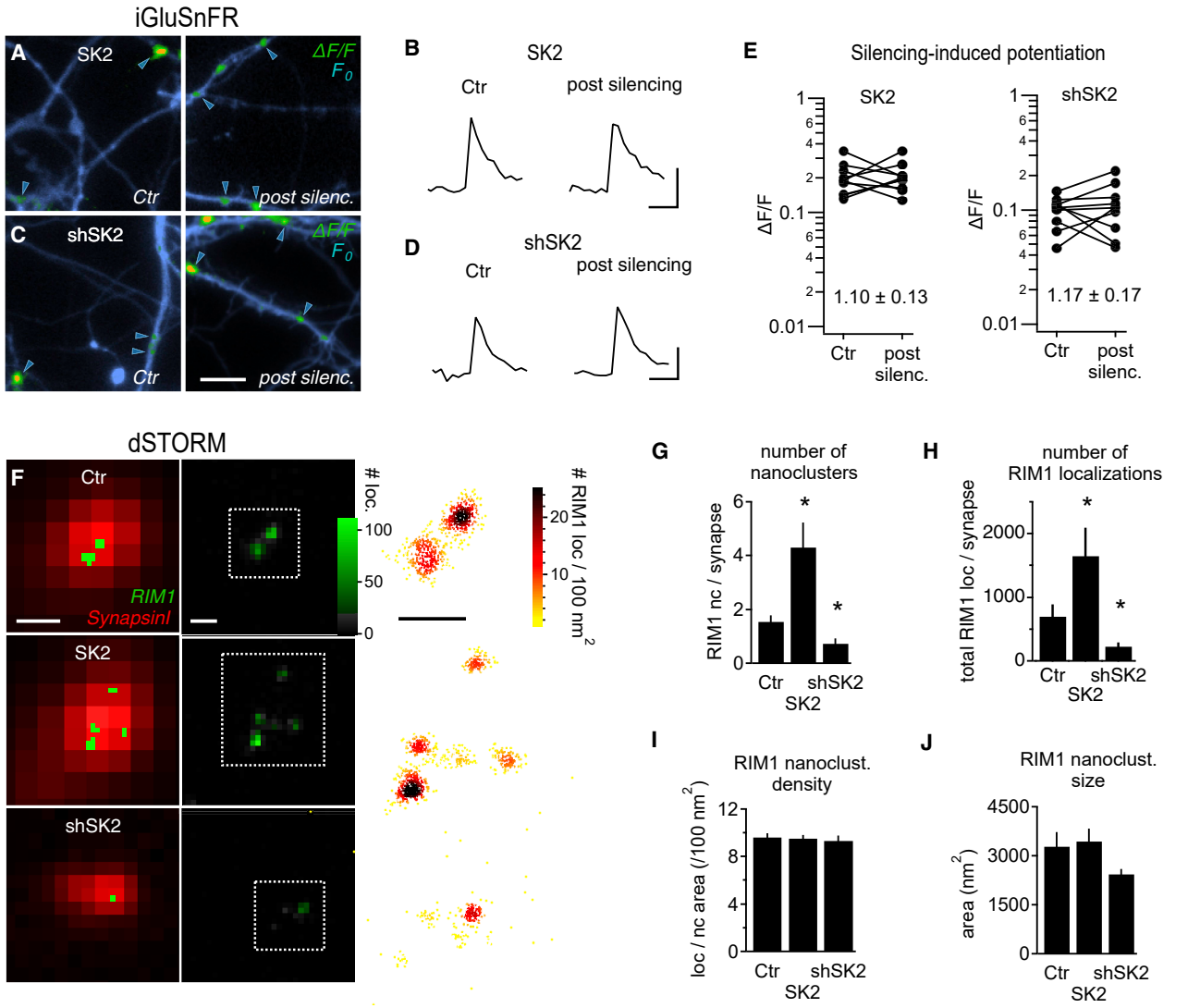


**Figure 4. SRPK2 is required for and occludes HP and increases the number of RIM1 nanoclusters in the presynapse**

(A and C) iGluSnFR expression (blue) with superimposed iGluSnFR ΔF/F responses (cf. Figure 1). Scale bar, 10 μm.

(B and D) Average iGluSnFR traces from experiments shown in (A) and (C). Scale bars: 100 ms, 10% and 100 ms, 5% for (B) and (D), respectively.

(E) Summary of iGluSnFR peak amplitudes. Lines denote paired experiments (n = 10 experiments for SK2 and shSK2 each, paired ratio t test). Numbers in the lower half of the panels denote the mean ± SEM of the individual post-silencing/Ctr ratios.

(F) Synapses transfected with GFP (Ctr), SRPK2-GFP (SK2), or shSRPK2-GFP (shSK2) and immunostained for Synapsin I (red, laser wide field). The left column shows dSTORM-based identification of RIM1 nanoclusters (green). Also shown are density histograms (center column) and density maps (r = 15 nm, right column) of RIM1 localizations. Scale bars from left to right: 200 nm, 100 nm, and 100 nm.

(G–J) Quantification of the number of RIM1 nanoclusters (G) and localizations per presynaptic bouton and of RIM1 nanocluster density (I) and size (J) in control (Ctr) (N = 6/6/6 cultures and n = 191, 216, and 249 synapses for Ctr, SK2, and shSK2, respectively. Significance was tested across cultures; ANOVA-HS 2 comp. against Ctr). (G), (H), (I), (J) Data are shown as mean ± SEM and differences were considered statistically significant if $p < 0.05$.

after silencing of SK2-expressing neurons; Figures 4A, 4B, and 4E) or decreased (1.17 ± 017-fold increase in signal amplitude; Figures 4C–4E). The shSRPK2 data suggest that the availability of SRPK2 molecules is essential for homeostatic regulation of release. The OE experiments indicate that the signaling pathways of PHP can be saturated by forced increases in synaptic SRPK2 levels so that further potentiation is occluded.

## SRPK2 increases the number of release-ready vesicles without changing the vesicular release probability

If SRPK2 triggers changes in release seen during HP, then it should also act by regulating RIM1 nanoclusters. We employed dSTORM and analyzed clustering of RIM1 molecules in presynaptic terminals of neurons transfected with Ctr, SRPK2, or shSRPK2 plasmids (Figures 4F–4J; STAR Methods). SRPK2 generated significantly more RIM1 nanoclusters (4.32 ± 0.92

and 1.54 ± 0.23 nanoclusters per synapse in SK2 and Ctr conditions, respectively), and KD of SRPK2 significantly decreased the number of RIM1 synaptic nanoclusters compared with Ctr (0.74 ± 0.19 nanoclusters per synapse in shSK2; Figure 4G and density maps in Figure 4F). The number of RIM1 localizations per synapse was significantly higher under the SK2 and lower in the KD condition (687 ± 188, 1,653 ± 443, and 229 ± 59 localizations per synapse in Ctr, SK2, and shSK2, respectively; Figure 4H). Neither the RIM1 density within nanoclusters nor the area of RIM1 nanoclusters were significantly changed by SRPK2 (Figures 4I and 4J), suggesting that SRPK2 is important for seeding but not growth of RIM1 nanoclusters.

To probe whether SRPK2 elevates the number of docked SVs per synapse, we three-dimensionally reconstructed synaptic terminals in image stacks acquired with focused ion beam scanning electron microscopy (FIB-SEM) from cultured neurons (Figures 5A–5C). We observed a clear and significant increase in the number of docked SVs following SRPK2 OE (5.41 ± 0.16, 8.49 ± 0.90, and 4.19 ± 0.38 docked SVs per synapse in Ctr and SK2- and shSK2-expressing neurons, respectively; Figures 5A and 5B), which was similar to the SRPK2-induced increase in RIM1 nanoclusters (Figure 4G). This increase was mirrored by a similar significant increase in the size of the postsynaptic density (0.039 ± 0.003, 0.069 ± 0.009, and 0.034 ± 0.001 postsynaptic density [PSD] area [$\mu m^2$] in Ctr and SK2- and shSK2-treated neurons, respectively; Figure 5C), indicating a concomitant expansion of presynaptic AZ size and suggesting that the postsynaptic receptor distribution matches the higher number of RIM nanoclusters and SVs (Hruska et al., 2015, 2018).

We employed a fluctuation analysis of iGluSnFr signal amplitudes to assess whether the SRPK2-induced augmentation in transmitter output may be due to an enlarged RRP or an elevated vesicular release probability (Huijstee and Kessels, 2020). Figures 5D–5F shows that SRPK2 induced a clear and significant increase in the inverse coefficient of variation (CV) calculated across a recording epoch but did not alter the variance-to-mean ratio (VMR). This situation is most consistent with an increase in RRP and an unchanged $P_r$ (Huijstee and Kessels, 2020). The constancy of VMR at augmented SRPK2 abundance also suggests that the optical amplitude in response to release of a single vesicle is not altered. Because optical responses are quantified as relative fluorescence increases (ΔF/F), their amplitude will be insensitive to any changes in the number or position of iGluSnFR sensor molecules, and the constancy of VMR here implies that the number of glutamate molecules per vesicle likely is not altered by SRPK2.

SRPK2 did not saturate transmitter output because elevating extracellular calcium to 4 mM potently and significantly increased the mean amplitude of iGluSnFR responses (Figures 5G–5I). 4 mM calcium augments responses by elevating the $P_r$. Thus, the pronounced additional increase in signals when applying 4 mM calcium in the presence of high levels of SRPK2 also supports the view that SRPK2 is not acting in the same way as high calcium but by enlarging the RRP.

## The SRPK2-dependent phosphoproteome includes AZ proteins and multiple kinases and phosphatases

To date, our knowledge about SRPK2 substrates is quite limited (Giannakouros et al., 2011). To identify presynaptic targets of SRPK2 involved in regulation of synaptic transmission, we performed a phosphoproteomics screen of cultured cortical neurons transduced with rAAV-SK2 and -shSK2 at 2–6 days *in vitro* (DIV) and processed them for MS at 14 DIV (Figure 6; Table S1). We quantified differential phosphorylation by comparing phosphorylated peptide species under the SRPK2 OE and KD condition with the untreated Ctr group (GFP only). Up- or downregulation of SRPK2 led to changes in the phosphorylation status of a large number of proteins (Figure 6A; Table S1; phosphopeptides with significantly changed phosphorylation status: 2823 SRPK2 OE, 1118 SRPK2 KD, and 382 under both conditions; Figure S8A).

Consistent with the established role of SRPK2 in regulation of alternative splicing in non-neuronal cells, proteins involved in this process constituted 10% of the 100 top hits in our phosphoproteomics screen. Unexpectedly, a Gene Ontology enrichment analysis of up- and downregulated phosphorylation sites revealed structural components of the AZ to be enriched (>7-fold OE, >4-fold KD) (Figure 6B).

An analysis of SRPK2-induced changes in the phosphorylation status of synaptic proteins using the SynGO database (Koopmans et al., 2019; Figures S8B and S8C) revealed that pre- and postsynaptic proteins were affected, in particular those belonging to the categories AZ, presynaptic membrane, and PSD. The phosphorylation status of fewer proteins was affected by KD (presynaptic, 7%; postsynaptic 5.7%) of SRPK2 than by OE (presynaptic and postsynaptic, 19%). This indicates that, under basal conditions, many potential SRPK2-regulated sites are not phosphorylated. RIM1 was the third most strongly regulated protein (Figure 6A; Table S1) and the AZ protein with the highest percentage of regulated phosphosites with respect to the amount of all potential phosphorylation sites (Figure 6C) and when correcting for protein size (Figure S8D). The phosphorylation status of the AZ members RIM-BP1, Liprin-α4, and Liprin-α1 was not regulated, and the other proteins showed a smaller degree of SRPK2-dependent change in phosphorylation status compared with RIM1 (Figure 6C). We also observed phosphorylation sites that were regulated inversely to the changes in SRPK2 levels, downregulated in OE and upregulated in KD (data not shown), consistent with a broader effect of SRPK2 on its interacting network of kinases and phosphatases (Figures 6D–6F).

## SRPK2 directly and indirectly regulates phosphorylation sites in RIM1

Our results so far suggest that SRPK2 affects synaptic strength by regulating the phosphorylation status of presynaptic RIM1 molecules, possibly via the phosphosites S991 and/or S1045, but our experiments do not provide direct evidence showing that SRPK2 causes phosphorylation of these sites. To test whether RIM1 is a direct SRPK2 substrate, we subjected purified $RIM1_{1–715}$ and $RIM1_{735–1615}$ to *in vitro* phosphorylation by SRPK2 and analyzed phosphorylated sites by radioactive *in vitro* phosphorylation (Figures S8E and S8F) and MS (Figures 6G; Table S1). We detected

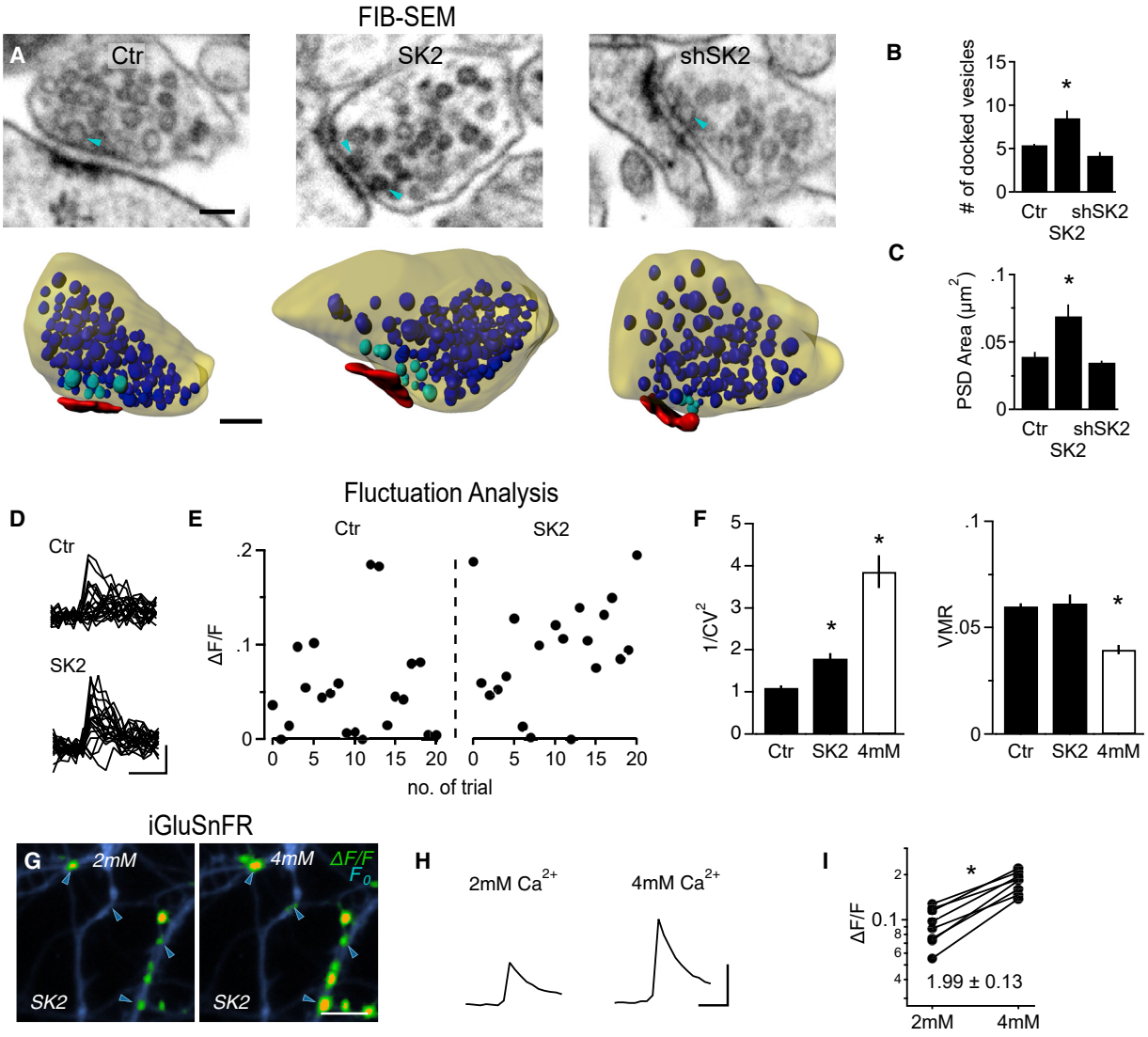


**Figure 5. SRPK2 increases the number of docked SVs**

(A) Example back-scattered electron images (top row) and reconstructed 3D synapses from the corresponding image stack (bottom row). Turquoise arrowheads in the top images mark some docked SVs. Color code for the 3D reconstructions: yellow, presynaptic membrane; dark blue, SVs; turquoise, docked SVs; red, PSD. Scale bars: 100 nm and 150 nm for the top and bottom row, respectively.

(B and C) Quantitative analysis of the number of docked SVs (B) and PSD area (C) per synapse in Ctr and SRPK2 OE and KD. N/n = 5/25, 6/40, and 5/34 for Ctr, SK2, and shSK2, respectively (cultures/synapses); ANOVA-HS 2 comp against Ctr.

(D–F) Statistical fluctuation analysis of the variability of stimulated synaptic iGluSnFR signal amplitudes (D). Scale bars: 100ms, 10%. $1/CV^2$, mean, and variance were calculated across recording epochs shown (E, peak amplitudes). Also shown is quantitative analysis of $1/CV^2$ (left graph) and of the variance-to-mean ratio (VMR, right graph) (F). n = 456, 207, and 89 synapses for Ctr (WT), SK2, and 4 mM $Ca^{2+}$, respectively; ANOVA-HS 2 comp against Ctr.

(G) iGluSnFR responses (green, cf. Figure 1) and baseline fluorescence (blue) of dKO neurons expressing *wt*RIM1 and SRPK2 in 2 and 4 mM extracellular $Ca^{2+}$. Scale bar, 10 µm.

(H) Average ΔF/F iGluSnFR traces of the experiment shown in (G). For this illustration, the mean ΔF/F traces (from 20 stimulations) of all analyzed ROIs (22) from the experiment in (G) were averaged. Scale bars: 100 ms, 10%.

(I) iGluSnFR peak response amplitudes for paired experiments recorded in 2 and 4 mM $Ca^{2+}$ (n = 8 experiments, paired ratio t test). (B), (C), (F), (I) Data are shown as mean ± SEM and differences were considered statistically significant if $p < 0.05$.

23 SRPK2-dependent phosphorylation sites in RIM1, which were found in the low-complexity linker regions between the zinc-finger and the PDZ domains and between the $C_2A$ domain and the PXXP motif but largely not in structural domains. Importantly, the vesicle release-relevant site $RIM1^{S1045}$ was identified as one of the direct SRPK2 target sites, whereas $RIM1^{S991}$ was not directly phosphorylated by SRPK2 in this *in vitro* assay.

To identify sites in RIM1 that are regulated by SRPK2 *in vivo*, we extracted all RIM1 phosphosites from our phosphoproteomics analysis of cultured neurons following SRPK2 OE or KD.

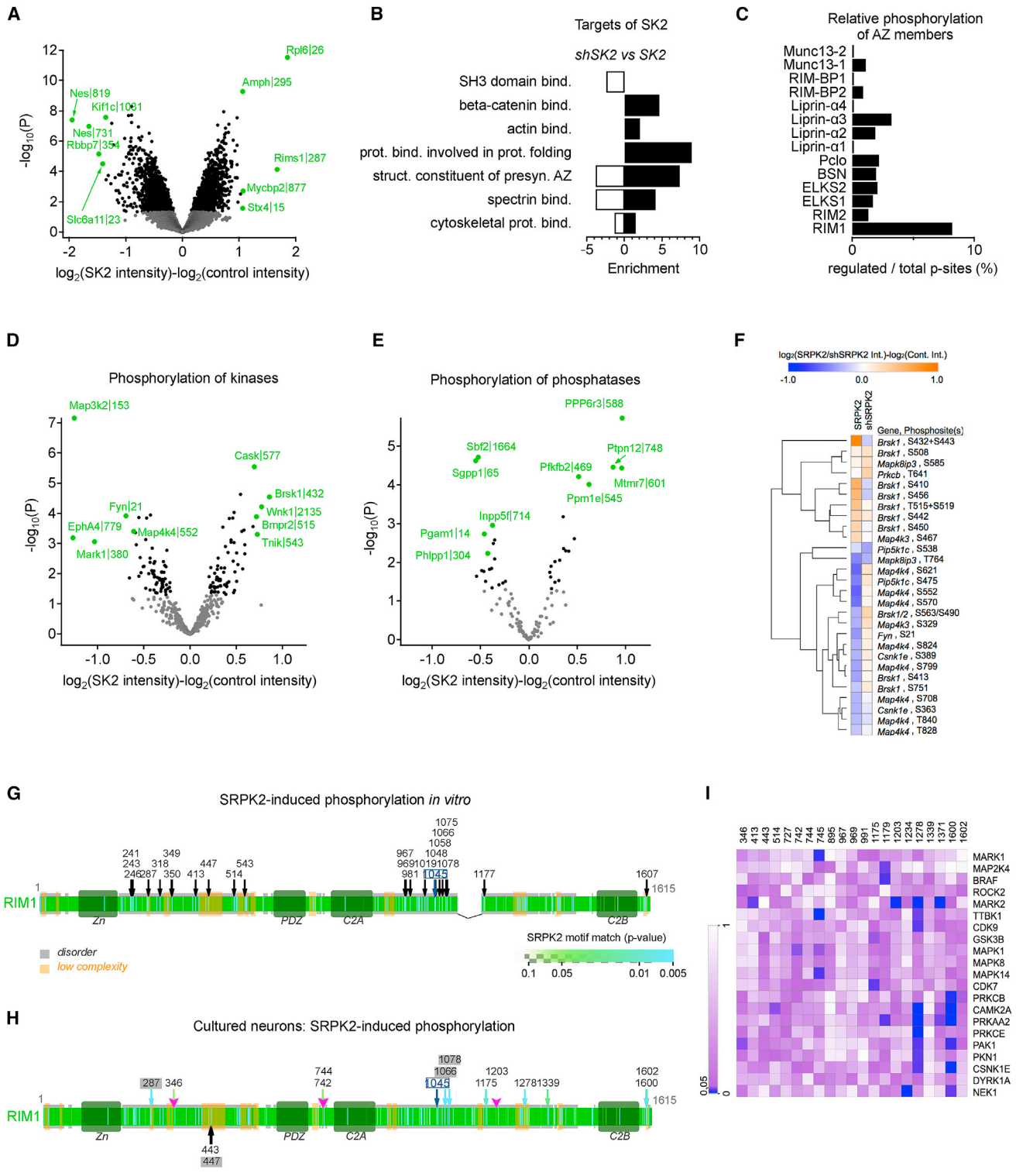


**Figure 6. Phosphoproteomics in neurons identifies synaptic proteins, kinases, and phosphatases as targets of SRPK2**

(A) Volcano plot showing differences in the phosphorylation status of all phosphopeptides after SRPK2 (SK2) OE compared with the Ctr condition (n = 5 cultures). Significant hits are shown in black, and the five most strongly regulated phosphorylation sites in either direction (up or down, excluding SRPK2) are indicated in green.

*(legend continued on next page)*

In this preparation we aimed to identify two types of SRPK2-regulated phosphosites in RIM1: first, sites that are targeted directly by SRPK2, and second, sites that are regulated by other kinases or phosphatases whose activity, in turn, is controlled by SRPK2. Consistent with the idea of RIM1$^{S1045}$ being a direct substrate of SRPK2, we found that this site was also regulated *in vivo* (Figure 6H). Four additional sites were identified *in vitro* and *in vivo* (S287, S447, S1066, and S1078), indicating that they, too, are direct target sites of SRPK2 in RIM1. RIM1$^{S991}$, the other site we found to be essential for RIM1's function in basal release, was not regulated in this preparation, suggesting that it is neither indirectly nor directly regulated by SRPK2 under the conditions used here. The comparison of the phosphorylation sites in RIM1 detected after *in vitro* phosphorylation (Figure 6G) with purified RIM1 or *in vivo* after manipulation of SRPK2 levels (Figure 6H) revealed many sites that were only found in one assay. This finding can be explained by the different experimental conditions; that is, the homogeneity of the *in vitro* sample subjected to phosphorylation versus phosphorylation *in vivo* in the presence of binding proteins, kinases, and phosphatases.

Based on the phosphorylation sites detected by the *in vitro* phosphorylation assay, a SRPK2 motif was deduced bioinformatically (Figure S8G; Table S2). This newly derived motif allowed us to map and determine the probabilities of potential SRPK2 target sites specific to RIM1 (Figure 6G, light green to blueish sticks on RIM), which also revealed a number of well-suited amino acid sites that were not affected by SRPK2 *in vitro* or *in vivo* (Figures 6G and 6H). It is possible that limited kinase access to these sites because of conformational constraints of RIM or interactions of RIM with other AZ proteins *in vivo* may play an important role (Figure 6H, light green to blueish sticks on RIM). Notably, sites in RIM that were found to be phosphorylated after SRPK2 treatment *in vivo* but not *in vitro* demonstrated insignificant matching to the derived SRPK2 motif, suggesting that those sites are indirectly regulated by SRPK2. SRPK2 directly phosphorylates RIM1 at multiple sites, one of which, S1045, is coupled to an increase in neurotransmitter release.

To explore which other kinases might be good candidates for indirect/non-exclusive phosphorylation of RIM, we listed all kinases that show SRPK2-regulated phosphosites (increase and/or decrease in OE and/or KD) and for which a consensus motif is known and calculated the probability of their motif matches to the phosphosites regulated in our *in vivo* assays (Figure 6I; Engholm-Keller et al., 2019).

## Silencing-induced plasticity and potentiation of release by SRPK2 are mimicked and occluded by RIM1$^{S1045E}$

If SRPK2 primarily acted via sites different from RIM1$^{S1045E}$, then it should still potentiate release irrespective of its phosphorylation status. We tested this by transducing RIM1/2 double-floxed neurons with lentiviruses expressing Cre recombinase and RIM1$^{S1045E}$ (or *wt*RIM1 as Ctr; Figures 7A and 7C). Although SRPK2 OE significantly increased release in *wt*RIM1-transduced neurons (Figure 7C, left black bar in the *wt*RIM1 group; 172% ± 24%, ΔF/F norm. to neurons only expressing *wt*RIM1), RIM1$^{S1045E}$ occluded the potentiating effect of SRPK2 on transmitter release. Release in the presence of SRPK2 and RIM1$^{S1045E}$ was maintained at the same high level (Figure 7C, left black bar of the 1045E group; 177% ± 37%, ΔF/F norm. to neurons expressing only *wt*RIM1), as was transmitter output in neurons expressing RIM1$^{S1045E}$ alone (Figure 7C, gray bar in the 1045E group).

We tested the involvement of RIM1$^{S1045E}$ in the silencing-induced increase in transmitter output in a similar way. Silencing increased release to ~160% (Figure 7C, right black bar of the *wt*RIM1 group; 158% ± 14%, ΔF/F norm. on non-silenced *wt*RIM1-expressing neurons), but TTX did not further augment transmitter output when cultures expressed RIM1$^{S1045E}$ (Figure 7C, right black bar in the 1045E group; 148% ± 15%, ΔF/F norm. on non-silenced *wt*RIM1-expressing neurons). These results strongly support the hypothesis that SRPK2's action on synaptic release and silencing-induced potentiation depend on phosphorylation of RIM1$^{S1045}$.

To address the possibility that sites other than S1045 may also occlude the action of SRPK2, we tested additional phospho-mutants of RIM1 (in RIM1/2 dKO neurons), targeted or not targeted by SRPK2, for their potential to alter transmitter release. Several mutants beyond S1045E and S991E increased release, as indicated by a rightshift along the x axis (Figure 7D; S895A, S1203E, and S514A; the gray area indicates the range of

(B) Gene Ontology enrichment analysis for all proteins showing significant changes in their phosphorylation status after SRPK2 OE (black bars) or SRPK2 KD (white bars). Enrichment refers to the number of proteins with significant changes in their phosphorylation status divided by the expected number of proteins for a specific category in the reference list (mouse proteins), GO (Pantherdb.org).

(C) Number of SRPK2-regulated phosphorylation sites in major constituents of the AZ normalized to the total number of all potential phosphorylation sites in the respective proteins as determined by NetPhos 3.1 (Blom et al., 2004).

(D and E) Volcano plots highlighting regulation phosphosites in kinases (D) and phosphatases (E) (significant hits in black).

(F) Hierarchical clustering of phosphorylation sites in synaptic scaling-associated protein kinases (Dörrbaum et al., 2020; Schanzenbächer et al., 2018) that were significantly regulated under the SRPK2 and shSRPK2 conditions. Sites were required to be significant under at least one of these conditions. The scale bar represents the difference in $\log_2$ intensity between the SRPK2 or shSRPK2 condition and their respective Ctr. This difference represents an upregulation (positive value) or a downregulation (negative value) upon SRPK2 OE or KD. Statistics for significantly regulated sites in (A) and (C–F): moderated t test.

(G) Schematic depicting RIM1 structural organization and phosphorylation sites identified by MS after *in vitro* phosphorylation of the fragments RIM$_{1–715}$ and RIM$_{735–1615}$ with purified SRPK2. The match with the SRPK2 consensus motif deduced from all phosphorylation sites (Figure S8G) is color coded, and the significance of the match is indicated by the color scale at the bottom (n = 4 independent replicates).

(H) Phosphosites whose phosphorylation status was altered by SRPK2 OE in primary neurons. Sites marked by gray boxes were identified *in vitro* and *in vivo*. The blue box highlights S1045, which is phosphorylated by SRPK2 *in vitro* and *in vivo* and can potentiate release. Pink arrows mark regulated sites with a very weak match to the SRPK2 consensus motif. A black arrow indicates downregulated di-phosphorylation of sites S443 and S447 (n = 5 cultures).

(I) Heatmap depicting the match of phosphosites indirectly regulated by SRPK2 (i.e., sites that were detected in the *in vivo* experiments but not in the *in vitro* experiments) to the consensus motifs of kinases (if known) whose phosphorylation status is altered by SRPK2 OE or KD. The color scheme indicates the probability of a match to the consensus motif.

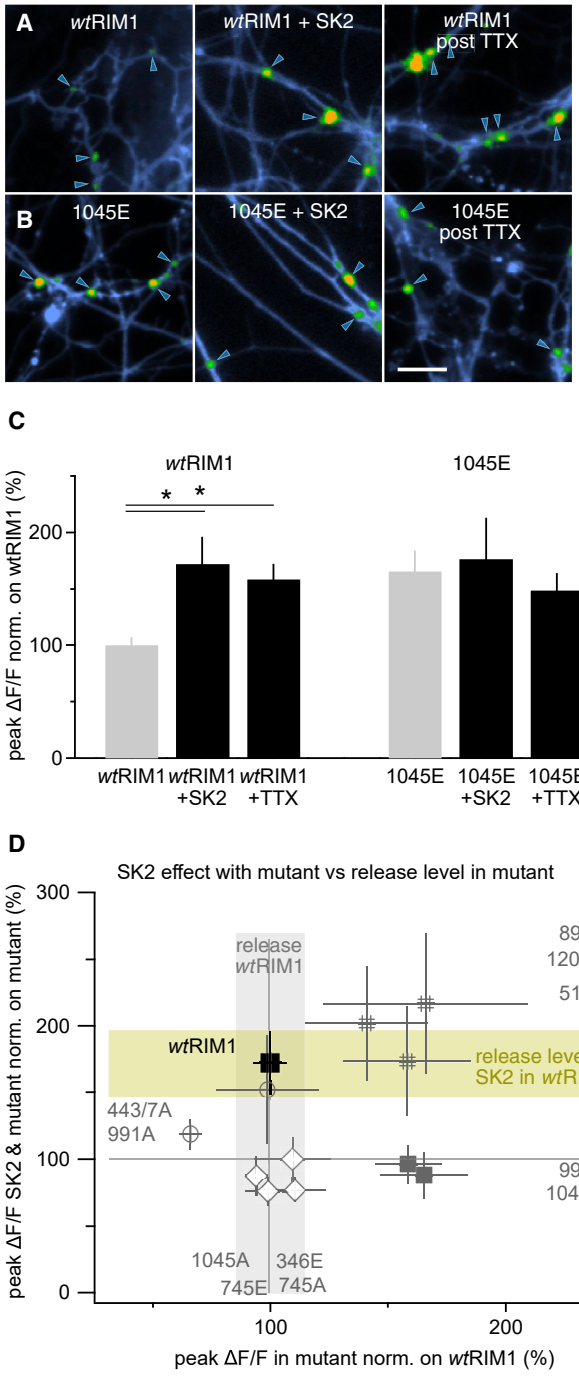


**Figure 7. SRPK2 action and PHP are occluded by RIM$^{S1045E}$**

(A and B) RIM dKO neurons expressing iGluSnFR (blue) in combination with iGluSnFR responses (ΔF/F). Scale bar, 10 μm.

(C) Summary of the experiments shown in (A) and (B). Mean iGluSnFR amplitudes were recorded under different conditions. The gray bars are reproduced from Figure 1 (number of experiments for black bars from left to right: n = 16, 11, 6, and 15; left bars, ANOVA-HS 2 comp. against WT RM1; right bars, ANOVA-HS 2 comp. against RIM1$^{S1045E}$).

(D) The potentiating effect of SRPK2 in the presence of a mutant (in the RIM1/2 dKO background, y axis) is plotted versus the effect of the mutant on release. The gray bar depicts the range of iGluSnFR responses observed in *wt*RIM1 neurons (black marker on the x axis). n = 3–23 experiments for each marker on both axes. (C) Data are shown as mean ± SEM and differences were considered statistically significant if $p < 0.05$.

iGluSnFR responses observed in *wt*RIM1 neurons). The comparison with cultures expressing SRPK2 and the mutant was used to test whether these mutant RIM1 proteins also occlude the functional effect of SRPK2. Those signal strengths are plotted on the y axis, and the yellow area indicates the range of transmitter release increase usually observed when SRPK2 is expressed in *wt*RIM1 cultures (Figure 7D). If the occlusion of the stimulatory effect of SRPK2 on release were generally due to a saturation phenomenon, then the points in this x,y plot should show an anti-correlation and a trend from the top left to the bottom right. This was not observed, but the individual mutants broadly formed 3 clusters. Members of the (S1045E, S991E) cluster, denoted by filled squares in Figure 7D, increase release on their own and prevent a further potentiating effect of SRPK2 (markers stay on the horizontal 100% line). This represents a classical occlusion phenomenon by a shared downstream mechanism with SRPK2 (e.g., enlarging the RRP) or by convergence on the RIM protein (the mutant site is operated by SRPK2). However, members of another cluster (S895A, S1203E, S514A; Figure 7D, hash marker) also elevated transmitter release to a similar degree (rightshifted from gray area) but still permitted an additional stimulatory effect of SRPK2 (Figure 7D, markers in and above the yellow area). Mutants of a third cluster (S1045A, S745A, S745E, S346E; Figure 7D, diamond) did not affect basal transmitter release (Figure 7D, in the gray area) but still occluded the effect of SRPK2 (Figure 7D, near horizontal gray line, no potentiation of SRPK2). These data mean that (1) the occlusion of SRPK2's stimulatory effect on release by S1045E cannot solely be explained by a saturating effect it may have on release (the hash cluster does not occlude) and (2) that the occlusion effect is not specific for S1045E and that other sites not controlled by SRPK2 (S991A/E, S745A/E, S346E) interfere with the action of SRPK2 on release. How individual mutant RIM1 proteins prevent, mimic, or add to the SRPK2-induced increase in synaptic release is explained in Figure S9.

## DISCUSSION

To date, it is still unresolved how RIM1 contributes to induction of presynaptic plasticity and how the activity of RIM1 in this process is regulated. It has been suggested that phosphorylation of RIM1 at S413 is a prerequisite for the protein to function in presynaptic plasticity (Lonart et al., 2003), but analysis of a knockin mouse with a S413A mutation did not substantiate this hypothesis (Kaeser et al., 2008). Our results demonstrate RIM1/2 to be essential for homeostatic upscaling of release and show that this form of plasticity is associated with an increase in the number of presynaptic RIM1 nanoclusters. We also found that regulation of the phosphorylation status of RIM1 at multiple sites (S1045, S991, S514, S895, and S1203) can potentiate neurotransmitter release. These results suggest that the signaling cascade upstream of RIM leads to formation of more release

sites (RIM nanoclusters) and, thereby, increases the number of docked SVs.

It is well established that the synaptic release probability correlates with the number of docked and release-ready vesicles (RRP) and that modulation of synaptic strength alters the size of the RRP and of the presynaptic AZ (Goda and Stevens, 1998; Matz et al., 2010; Moulder et al., 2004; Murthy et al., 2001; Schikorski and Stevens, 1997, 2001; Weyhersmuller et al., 2011). Here we demonstrate that these parameters can be tuned by increasing the level of the kinase SRPK2. SRPK2 regulates $P_r$ by increasing the number of readily releasable vesicles per synapse in a RIM1-dependent manner. Because higher SRPK2 levels cause lengthening of the PSD, SRPK2-triggered changes in $P_r$ most likely also result in a larger AZ (Sanderson et al., 2018). Our findings also support the notion that modulation of synaptic strength by SRPK2 contributes to the homeostatic response to changes in neuronal network activity. Our KD experiments show that SRPK2 is required for induction of PHP. Occlusion of TTX-mediated homeostatic upscaling after SRPK2 OE, on the other hand, suggests that OE maximally activates the signaling pathways coupled to HP so that silencing cannot increase transmitter release any further. This SRPK2 occlusion effect could be explained mechanistically by saturating the level of phosphorylation of presynaptic RIM1 molecules at S1045 and other sites indirectly regulated by SRPK2.

We found that increasing the abundance of SRPK2 stimulates glutamate release. Taking into consideration that PHP is not associated with an increase in the number of presynaptic SRPK2 molecules or nanoclusters (Figure S10), this suggests that the mechanism underlying the increase in synaptic transmission during PHP and SRPK2 OE may not be completely identical in all respects and that PHP might have a broader action range than SRPK2. As mentioned above, chronic neuronal silencing triggers translation and phosphorylation of multiple kinases and phosphatases as well as a large number of pre- and postsynaptic proteins (Desch et al., 2021; Dörrbaum et al., 2020; Schanzenbächer et al., 2016, 2018), which will likely affect the presynaptic release machinery and, thereby, release at multiple levels. The signaling cascade activated by SRPK2 OE was more restricted. This is evidenced, for example, by the fact that not all of the kinases regulated by PHP (Dörrbaum et al., 2020; Schanzenbächer et al., 2018) are altered by SRPK2 OE and KD (Figure 6F).

In this study, we identified several sites in RIM1 whose phosphorylation status is important for neurotransmitter output. Remarkably, we observed a pronounced increase in glutamate release even when RIM1 was modified at only a single serine (e.g., 991, 1,045, 514, 895, 1,203). The degree of this potentiation was around 70%, a level commonly observed during LTP, suggesting that such potentiation could be reached by phosphorylation of individual residues. Depending on the site, a stimulatory effect on synaptic transmission resulted from phospho-mimic (991, 1,045, 1,203) or phospho-deficient (514, 895) modifications. A decrease in glutamate release was detected only for $RIM1^{S991A}$. The fact that we found by far fewer sites that downregulated release may be explained by a scenario where, under basal conditions, the serines remain in the unphosphorylated state, not making use of the potential to increase release. This would suggest that the phosphorylated state is not essential for basal release but mainly engaged to positively modulate it. It also has to be considered that *in vivo* phosphorylation sites are dynamically regulated in a combinatorial manner and that "loss" of one site might be compensated. Alternatively, there might be an intrasynaptic homeostatic regulation enforcing stronger incorporation of release-inefficient RIM1 mutants into the AZ to maintain a certain level of transmission so that a negative effect on release of a mutant tends to be compensated.

Our map of release-relevant or regulatory phosphorylation sites demarcates phospho-domains in the RIM1 protein and shows how kinases and phosphatases can cooperate or compete with each other by acting on RIM1 to achieve complex, possibly temporal, regulatory scenarios of transmitter release. Our data contribute to dissecting and deciphering the importance of protein-protein interactions of RIM1, using the mutants we validated as a tool to probe the importance of individual sites for interactions.

Our combination of functionally assaying glutamate release in combination with expression of a number of different phospho-mutants in RIM1/2 dKO cells suggests that there are several functional phospho-domains in RIM1; phosphorylation in some domains of RIM1 promotes or inhibits release, whereas other domains seem to be of regulatory importance for controlling the functional outcome of the actions of kinases on RIM1. RIM1 potentially interacts with a large number of other presynaptic proteins, and we envisage that the phosphorylation state of amino acids in certain functional RIM1 domains directly affects protein interactions or leads to steric or conformational changes of the RIM1 protein, which, in turn, could affect its function, its interactions, and its modifiability by other kinases.

All sites in RIM1 we examined with regard to their functional relevance have been identified as being regulated by neuronal activity after a brief stimulation of neurons and synaptosomes with high KCl (Engholm-Keller et al., 2019; Kohansal-Nodehi et al., 2016) or after 24 h of presynaptic silencing (Desch et al., 2021). However, the complexity of phospho-regulation is evidenced by the observation in the same studies that sites can be altered in the same direction by paradigms that trigger an opposing functional outcome; S1203 phosphorylation, for example, is increased after 24 h of TTX and gabazine treatment. On the other hand, S1045, which, in its phospho-mimic variant, can occlude PHP, was not found to be differentially phosphorylated after chronic activity blockade (Desch et al., 2021). This might indicate that constitutive phosphorylation of S1045 is necessary for induction of PHP or that its phosphorylation status is altered at a time point during silencing that was not analyzed by Desch et al. (2021). It will therefore be important to obtain a better understanding of the changes occurring during chronic activity blockade and to resolve how the phosphorylation code of one RIM1 molecule is affected at different time points.

Our results have identified SRPK2 as a key signaling molecule for induction of PHP at mammalian synapses and RIM1 as the major effector protein of SRPK2 at the AZ and an essential player in this type of plasticity. SRPK2-induced phosphorylation of S1045 in RIM1 is essential and sufficient alone to increase the level of glutamate release, likely by triggering formation of novel RIM1 nanoclusters and release sites filled with SVs in the presynapse. Our data show that RIM1's function in release is regulated by a

complex phosphorylation code involving multiple phosphorylation events and multiple kinases.

### Limitations of the study

PHP *in vitro* is a robust and frequently applied paradigm for inducing prominent changes in the strength of synaptic transmission, but it should be noted that the *in vivo* triggers of HP may be more subtle and more transient (compared with 2 days of TTX silencing) as well as more diverse. Thus, although our study provides mechanistic insight into PHP, it cannot be transferred one to one to the *in vivo* situation, and most likely the underlying mechanisms and processes will be more diverse under physiological conditions.

A number of our experiments that address the functional roles of specific phosphorylation sites in the RIM1 protein make use of amino acid substitutions to yield mutant RIM1 proteins mimicking a phosphorylated or non-phosphorylated state by substituting glutamic acid (E) or alanine (A) for serines. Although this is a commonly used approach, it should be noted that these mutant proteins may not in all aspects behave like non-phosphorylated or phosphorylated serines.

Our phosphoproteomics approach, as all such studies, is based on comparing relative amounts of phospho-peptides between conditions. The data do not yield information about the absolute levels or the abundance of individual phospho-peptides. A phosphorylated site for which we do not detect regulation can be of low, medium, or high abundance.

## STAR★METHODS

Detailed methods are provided in the online version of this paper and include the following:

- KEY RESOURCES TABLE
- RESOURCE AVAILABILITY
  - Lead contact
  - Materials availability
  - Data and code availability
- EXPERIMENTAL MODEL AND SUBJECT DETAILS
  - Animals
  - Neuronal cell cultures
  - HEK293T cells
- METHOD DETAILS
  - Antibodies
  - Viral vector production
  - Constructs
  - Subcellular fractionation
  - Protein purification from HEK293T cells
  - Fluorescent protein lysate preparation from HEK293T cells
  - Subcellular fractionation
  - Immunoblotting
  - Crude synaptosome preparation and binding assay with subsequent MS analysis
  - Immunoprecipitation and GST-pull down
  - *In vitro* phosphorylation
  - Mass spectrometry of primary neurons
  - Mass spectrometry of *in vitro* phosphorylated RIM1
  - Immunohistochemistry of primary neurons
  - Immunohistochemistry of HEK293T cells
  - Confocal imaging and analysis
  - Direct stochastic optical reconstruction microscopy (dSTORM)
  - Electron microscopy
  - Two-photon fluorescence lifetime imaging microscopy (FLIM)
  - FM4-64 styryl dye imaging experiments
  - iGluSnFR experiments
- QUANTIFICATION AND STATISTICAL ANALYSIS
  - dSTORM nanocluster analysis
  - Electron microscopy
  - Analysis of FM4-64 styryl dye imaging experiments
  - Analysis of iGluSnFR experiments
  - FLIM analysis
  - Processing of maxquant data
  - Protein kinase substrate prediction
  - SRPK2 motif
  - *In silico* RIM1 – SRPK profile
  - Statistical analysis of data

### SUPPLEMENTAL INFORMATION

Supplemental information can be found online at https://doi.org/10.1016/j.celrep.2022.110696.

### ACKNOWLEDGMENTS

We are grateful to M. Missler for help with EM sample preparation, Karen van Loo for assistance with GO analysis, and M. Geyer and R. Düster for technical assistance with *in vitro* phosphorylation assays. Our work was supported by the German Research Foundation (SFB1089, SP1775, and SCHO 820/4-7 to S.S. and D.D. and INST1172 15, DI853/3-5 and -7 and INST 217/785-1 to D.D.), the BONFOR program of the University of Bonn Medical Center (to S.S. and D.D.), a National Health and Medical Research Project Grant (1079160 to M.E.G.), the Cancer Institute New South Wales and the Australian Cancer Research Foundation, Australia (to M.E.G.). We would like to acknowledge the assistance of the Imaging, Proteomics, and Viral Core Facilities (supported by SFB1089) of the University Hospital Bonn. We thank S. Opitz, P. Trebing, and K. Krischer for excellent technical assistance. We acknowledge the support of the Children's Medical Research Institute Biomedical Proteomics Facility.

### AUTHOR CONTRIBUTIONS

Conceptualization, S.S. and D.D.; experimental design, J.A.M., J.B., M.E.G., D.D., and S.S.; investigation, J.A.M., J.B., K.E.-K., A.-M.O., A.M., I.P., J.S.-T., E.S., P.G., and J.R.W.; data analysis, J.A.M., J.B., A.-M.O., A.M., I.P., E.S., P.G., A.J.W., M.E.G., L.J.G., and T.D.M.; software development, T.D.M., L.J.G., and D.D.; supervision, A.J.B., M.E.G., D.D., and S.S.; funding acquisition, A.J.B., A.L., A.J.W., M.E.G., D.D., and S.S. J.A.M., J.B., A.J.W., M.E.G., D.D., and S.S. designed figures and wrote the manuscript with input from all authors.

### DECLARATION OF INTERESTS

The authors declare no competing interests.

Received: November 2, 2020
Revised: November 26, 2021
Accepted: March 29, 2022
Published: April 19, 2022

## REFERENCES


Benjamini, Y., and Hochberg, Y. (1995). Controlling the false discovery rate: a practical and powerful approach to multiple testing. J. R. Stat. Soc. Ser. B Methodol. *57*, 289–300.

Blom, N., Sicheritz-Pontén, T., Gupta, R., Gammeltoft, S., and Brunak, S. (2004). Prediction of post-translational glycosylation and phosphorylation of proteins from the amino acid sequence. Proteomics *4*, 1633–1649.

Buzsáki, G. (2010). Neural syntax: cell assemblies, synapsembles, and readers. Neuron *68*, 362–385.

Campbell, R.E., Tour, O., Palmer, A.E., Steinbach, P.A., Baird, G.S., Zacharias, D.A., and Tsien, R.Y. (2002). A monomeric red fluorescent protein. Proc. Natl. Acad. Sci. U S A *99*, 7877–7882.

Castillo, P.E., Schoch, S., Schmitz, F., Südhof, T.C., and Malenka, R.C. (2002). RIM1alpha is required for presynaptic long-term potentiation. Nature *415*, 327–330.

Chen, H., Tang, A.-H., and Blanpied, T.A. (2018). Subsynaptic spatial organization as a regulator of synaptic strength and plasticity. Curr. Opin. Neurobiol. *51*, 147–153.

Cull-Candy, S.G., Miledi, R., Trautmann, A., and Uchitel, O.D. (1980). On the release of transmitter at normal, myasthenia gravis and myasthenic syndrome affected human end-plates. J. Physiol. *299*, 621–638.

Daub, H., Blencke, S., Habenberger, P., Kurtenbach, A., Dennenmoser, J., Wissing, J., Ullrich, A., and Cotten, M. (2002). Identification of SRPK1 and SRPK2 as the major cellular protein kinases phosphorylating hepatitis B virus core protein. J Virol *76*, 8124–8137.

Davis, G.W., and Müller, M. (2015). Homeostatic control of presynaptic neurotransmitter release. Annu. Rev. Physiol. *77*, 251–270.

Delvendahl, I., and Müller, M. (2019). Homeostatic plasticity-a presynaptic perspective. Curr. Opin. Neurobiol. *54*, 155–162.

Deng, L., Kaeser, P.S., Xu, W., and Südhof, T.C. (2011). RIM proteins activate vesicle priming by reversing autoinhibitory homodimerization of Munc13. Neuron *69*, 317–331.

Desch, K., Langer, J.D., and Schuman, E.M. (2021). Dynamic bi-directional phosphorylation events associated with the reciprocal regulation of synapses during homeostatic up- and down-scaling. Cell Rep. *36*, 109583.

Dörrbaum, A.R., Alvarez-Castelao, B., Nassim-Assir, B., Langer, J.D., and Schuman, E.M. (2020). Proteome dynamics during homeostatic scaling in cultured neurons. Elife *9*, e52939.

Duarte, M., Wang, L., Calderwood, M.A., Adelmant, G., Ohashi, M., Roecklein-Canfield, J., Marto, J.A., Hill, D.E., Deng, H., and Johannsen, E. (2013). An RS motif within the Epstein-Barr virus BLRF2 tegument protein is phosphorylated by SRPK2 and is important for viral replication. Plos One *8*, e53512.

Dudoit, S., Yang, Y.H., Callow, M.J., and Speed, T.P. (2002). Statistical methods for identifying differentially expressed genes in replicated cDNA microarray experiments. Stat. Sin. *12*, 111–139.

Dürst, C.D., Wiegert, J.S., Helassa, N., Kerruth, S., Coates, C., Schulze, C., Geeves, M.A., Török, K., and Oertner, T.G. (2019). High-speed imaging of glutamate release with genetically encoded sensors. Nat Protoc *14*, 1401–1424.

Engholm-Keller, K., Waardenberg, A.J., Müller, J.A., Wark, J.R., Fernando, R.N., Arthur, J.W., Robinson, P.J., Dietrich, D., Schoch, S., and Graham, M.E. (2019). The temporal profile of activity-dependent presynaptic phospho-signalling reveals long-lasting patterns of poststimulus regulation. PLoS Biol. *17*, e3000170.

Fisher, S.R.A. (1956). Statistical methods for research workers. by sir Ronald A. Fisher. Edinburgh (Oliver and Boyd). Q. J. R. Meteorol. Soc. *82*, 119.

Fourcaudot, E., Gambino, F., Humeau, Y., Casassus, G., Shaban, H., Poulain, B., and Lüthi, A. (2008). cAMP/PKA signaling and RIM1alpha mediate presynaptic LTP in the lateral amygdala. Proc. Natl. Acad. Sci. U S A *105*, 15130–15135.

Frank, C.A., James, T.D., and Müller, M. (2020). Homeostatic control of Drosophila neuromuscular junction function. Synapse *74*, e22133.

Genç, Ö., An, J.Y., Fetter, R.D., Kulik, Y., Zunino, G., Sanders, S.J., and Davis, G.W. (2020). Homeostatic plasticity commonly fails at the intersection of autism-gene mutations and a novel class of common phenotypic modifier. Preprint at bioRxiv, 2020.01.31.927665.

Gentleman, R.C., Carey, V.J., Bates, D.M., Bolstad, B., Dettling, M., Dudoit, S., Ellis, B., Gautier, L., Ge, Y., Gentry, J., et al. (2004). Bioconductor: open software development for computational biology and bioinformatics. Genome Biol. *5*, R80.

Giannakouros, T., Nikolakaki, E., Mylonis, I., and Georgatsou, E. (2011). Serine-arginine protein kinases: a small protein kinase family with a large cellular presence. FEBS J. *278*, 570–586.

Goda, Y., and Stevens, C.F. (1998). Readily releasable pool size changes associated with long term depression. Proc. Natl. Acad. Sci. U S A *95*, 1283–1288.

Han, Y., Kaeser, P.S., Südhof, T.C., and Schneggenburger, R. (2011). RIM determines Ca2+ channel density and vesicle docking at the presynaptic active zone. Neuron *69*, 304–316.

Hruska, M., Henderson, N.T., Xia, N.L., Marchand, S.J.L., and Dalva, M.B. (2015). Anchoring and synaptic stability of PSD-95 is driven by ephrin-B3. Nat. Neurosci. *18*, 1594–1605.

Hong, Y., Chan, C.B., Kwon, I.-S., Li, X., Song, M., Lee, H.-P., Liu, X., Sompol, P., Jin, P., Lee, H., et al. (2012). SRPK2 phosphorylates tau and mediates the cognitive defects in Alzheimer's disease. The Journal of Neuroscience : The Official Journal of the Society for Neuroscience *32*, 17262–17272.

Hruska, M., Henderson, N., Marchand, S.J.L., Jafri, H., and Dalva, M.B. (2018). Synaptic nanomodules underlie the organization and plasticity of spine synapses. Nat. Neurosci. *21*, 671–682.

Huijstee, A.N.V., and Kessels, H.W. (2020). Variance analysis as a tool to predict the mechanism underlying synaptic plasticity. J. Neurosci. Methods *331*, 108526.

Kaeser, P.S., Kwon, H.-B., Blundell, J., Chevaleyre, V., Morishita, W., Malenka, R.C., Powell, C.M., Castillo, P.E., and Südhof, T.C. (2008). RIM1alpha phosphorylation at serine-413 by protein kinase A is not required for presynaptic long-term plasticity or learning. Proc. Natl. Acad. Sci. U S A *105*, 14680–14685.

Jang, S.-W., Yang, S.-J., Ehlén, A., Dong, S., Khoury, H., Chen, J., Persson, J.L., and Ye, K. (2008). Serine/arginine protein-specific kinase 2 promotes leukemia cell proliferation by phosphorylating acinus and regulating cyclin A1. Cancer Research *68*, 4559–4570.

Kaeser, P.S., Deng, L., Wang, Y., Dulubova, I., Liu, X., Rizo, J., and Südhof, T.C. (2011). RIM proteins tether Ca2+ channels to presynaptic active zones via a direct PDZ-domain interaction. Cell *144*, 282–295.

Kohansal-Nodehi, M., Chua, J.J., Urlaub, H., Jahn, R., and Czernik, D. (2016). Analysis of protein phosphorylation in nerve terminal reveals extensive changes in active zone proteins upon exocytosis. ELife *5*, e14530.

Koopmans, F., Nierop, P.V., Andres-Alonso, M., Byrnes, A., Cijsouw, T., Coba, M.P., Cornelisse, L.N., Farrell, R.J., Goldschmidt, H.L., Howrigan, D.P., et al. (2019). SynGO: an evidence-based, expert-curated knowledge Base for the synapse. Neuron *103*, 217–234.e4.

Lazarevic, V., Schone, C., Heine, M., Gundelfinger, E.D., and Fejtova, A. (2011). Extensive remodeling of the presynaptic cytomatrix upon homeostatic adaptation to network activity silencing. J. Neurosci. *31*, 10189–10200.

Leek, J.T., and Storey, J.D. (2007). Capturing heterogeneity in gene expression studies by surrogate variable analysis. PLoS Genet. *3*, e161.

Liang, N., Zeng, C., Tao, K.P., Sou, W.H., Hsia, H.P., Qu, D., Lau, S.N., and Ngo, J.C. (2014). Primary structural features of SR-like protein acinusS govern the phosphorylation mechanism by SPRK2. Biochem. J. *459*, 181–191.

Lignani, G., Baldelli, P., and Marra, V. (2020). Homeostatic plasticity in epilepsy. Front. Cell. Neurosci. *14*, 197.

Loo, K.M.J., van Schaub, C., Pernhorst, K., Yaari, Y., Beck, H., Schoch, S., and Becker, A.J. (2012). Transcriptional regulation of T-type calcium channel CaV3.2: bi-directionality by early growth response 1 (Egr1) and repressor element 1 (RE-1) protein-silencing transcription factor (REST). Journal of Biological Chemistry *287*, 15489–15501.

Loo, K.M.J., van Rummel, C.K., Pitsch, J., Müller, J.A., Bikbaev, A.F., Chavez, E.M., Blaess, S., Dietrich, D., Heine, M., Becker, A.J., et al. (2019). Calcium channel subunit α2δ4 is regulated by early growth response 1 and facilitates epileptogenesis. The Journal of Neuroscience : The Official Journal of the Society for Neuroscience *39*, 1731-18–3187.

Lonart, G., Schoch, S., Kaeser, P.S., Larkin, C.J., Südhof, T.C., and Linden, D.J. (2003). Phosphorylation of RIM1alpha by PKA triggers presynaptic long-term potentiation at cerebellar parallel fiber synapses. Cell *115*, 49–60.

Marder, E., and Prinz, A.A. (2002). Modeling stability in neuron and network function: the role of activity in homeostasis. Bioessays *24*, 1145–1154.

Marvin, J.S., Borghuis, B.G., Tian, L., Cichon, J., Harnett, M.T., Akerboom, J., Gordus, A., Renninger, S.L., Chen, T.-W., Bargmann, C.I., et al. (2013). An optimized fluorescent probe for visualizing glutamate neurotransmission. Nat. Methods *10*, 162–170.

Marvin, J.S., Scholl, B., Wilson, D.E., Podgorski, K., Kazemipour, A., Müller, J.A., Schoch, S., Quiroz, F.J.U., Rebola, N., Bao, H., et al. (2018). Stability, affinity, and chromatic variants of the glutamate sensor iGluSnFR. Nat. Methods. *15*, 936–939.

Matsuda, T., and Cepko, C.L. (2007). Controlled expression of transgenes introduced by in vivo electroporation. Proc. Natl. Acad Sci. U S A *104*, 1027–1032.

Matz, J., Gilyan, A., Kolar, A., McCarvill, T., and Krueger, S.R. (2010). Rapid structural alterations of the active zone lead to sustained changes in neurotransmitter release. Proc. Natl. Acad. Sci. U S A *107*, 8836–8841.

Miller, K.D. (1996). Synaptic economics: competition and cooperation in synaptic plasticity. Neuron *17*, 371–374.

Moulder, K.L., Meeks, J.P., Shute, A.A., Hamilton, C.K., Erausquin, G.D., and Mennerick, S. (2004). Plastic elimination of functional glutamate release sites by depolarization. Neuron *42*, 423–435.

Müller, M., Liu, K.S.Y., Sigrist, S.J., and Davis, G.W. (2012). RIM controls homeostatic plasticity through modulation of the readily-releasable vesicle pool. J. Neurosci. *32*, 16574–16585.

Murthy, V.N., Schikorski, T., Stevens, C.F., and Zhu, Y. (2001). Inactivity produces increases in neurotransmitter release and synapse size. Neuron *32*, 673–682.

Nahidiazar L, Agronskaia AV, Broertjes J, van den Broek B, Jalink K. Optimizing Imaging Conditions for Demanding Multi-Color Super Resolution Localization Microscopy. PLoS One. 2016 Jul 8;11(7):e0158884. https://doi.org/10.1371/journal.pone.0158884. PMID: 27391487; PMCID: PMC4938622.

Orr, B.O., Hauswirth, A.G., Celona, B., Fetter, R.D., Zunino, G., Kvon, E.Z., Zhu, Y., Pennacchio, L.A., Black, B.L., and Davis, G.W. (2020). Presynaptic homeostasis opposes disease progression in mouse models of ALS-Like degeneration: evidence for homeostatic neuroprotection. Neuron *107*, 95–111.e6.

Pelkey, K.A., Topolnik, L., Yuan, X.-Q., Lacaille, J.-C., and McBain, C.J. (2008). State-dependent cAMP sensitivity of presynaptic function underlies metaplasticity in a hippocampal feedforward inhibitory circuit. Neuron *60*, 980–987.

Poo, M., Pignatelli, M., Ryan, T.J., Tonegawa, S., Bonhoeffer, T., Martin, K.C., Rudenko, A., Tsai, L.-H., Tsien, R.W., Fishell, G., et al. (2016). What is memory? the present state of the engram. BMC Biol. *14*, 40.

Ritchie, M.E., Phipson, B., Wu, D., Hu, Y., Law, C.W., Shi, W., and Smyth, G.K. (2015). Limma powers differential expression analyses for RNA-sequencing and microarray studies. Nucleic Acids Res. *43*, e47.

Sanderson, T.M., Bradley, C.A., Georgiou, J., Hong, Y.H., Ng, A.N., Lee, Y., Kim, H.-D., Kim, D., Amici, M., Son, G.H., et al. (2018). The probability of neurotransmitter release governs AMPA receptor trafficking via activity-dependent regulation of mGluR1 surface expression. Cell Rep. *25*, 3631–3646.e3.

Schanzenbächer, C.T., Sambandan, S., Langer, J.D., and Schuman, E.M. (2016). Nascent proteome remodeling following homeostatic scaling at hippocampal synapses. Neuron *92*, 358–371.

Schanzenbächer, C.T., Langer, J.D., and Schuman, E.M. (2018). Time- and polarity-dependent proteomic changes associated with homeostatic scaling at central synapses. ELife *7*, 489.

Schikorski, T., and Stevens, C.F. (1997). Quantitative ultrastructural analysis of hippocampal excitatory synapses. J. Neurosci. *17*, 5858–5867.

Schikorski, T., and Stevens, C.F. (2001). Morphological correlates of functionally defined synaptic vesicle populations. Nat. Neurosci. *4*, 391–395.

Schneider, T.D., and Stephens, R.M. (1990). Sequence logos: a new way to display consensus sequences. Nucleic Acids Res *18*, 6097–6100.

Schoch, S., Castillo, P.E., Jo, T., Mukherjee, K., Geppert, M., Wang, Y., Schmitz, F., Malenka, R.C., and Südhof, T.C. (2002). RIM1alpha forms a protein scaffold for regulating neurotransmitter release at the active zone. Nature *415*, 321–326.

Schoch, S., Mittelstaedt, T., Kaeser, P.S., Padgett, D., Feldmann, N., Chevaleyre, V., Castillo, P.E., Hammer, R.E., Han, W., Schmitz, F., et al. (2006). Redundant functions of RIM1alpha and RIM2alpha in Ca(2+)-triggered neurotransmitter release. EMBO J. *25*, 5852–5863.

Tang, A.-H., Chen, H., Li, T.P., Metzbower, S.R., MacGillavry, H.D., and Blanpied, T.A. (2016). A trans-synaptic nanocolumn aligns neurotransmitter release to receptors. Nature *536*, 210–214.

Turrigiano, G.G., and Nelson, S.B. (2004). Homeostatic plasticity in the developing nervous system. Nat. Rev. Neurosci. *5*, 97–107.

Turrigiano, G.G., Leslie, K.R., Desai, N.S., Rutherford, L.C., and Nelson, S.B. (1998). Activity-dependent scaling of quantal amplitude in neocortical neurons. Nature *391*, 892–896.

Vivarelli, S., Lenzken, S.C., Ruepp, M.-D., Ranzini, F., Maffioletti, A., Alvarez, R., Mühlemann, O., and Barabino, S.M.L. (2013). Paraquat modulates alternative Pre-mRNA splicing by modifying the intracellular distribution of SRPK2. PLoS One. *8*, e61980.

Waardenberg, A.J. (2017). Methods in molecular biology. Methods Mol. Biol. *1599*, 229–244.

Wang, F., Fu, X., Chen, P., Wu, P., Fan, X., Li, N., Zhu, H., Jia, T.-T., Ji, H., Wang, Z., et al. (2017). SPSB1-mediated HnRNP A1 ubiquitylation regulates alternative splicing and cell migration in EGF signaling. Cell Res *27*, 540–558.

Wessel, D., and Flügge, U.I. (1984). A method for the quantitative recovery of protein in dilute solution in the presence of detergents and lipids. Anal. Biochem. *138*, 141–143.

Weyhersmuller, A., Hallermann, S., Wagner, N., and Eilers, J. (2011). Rapid active zone remodeling during synaptic plasticity. J. Neurosci. *31*, 6041–6052.

Zhuang, X., Wong, N.F., Sun, W., and Xu-Friedman, M.A. (2020). Mechanisms and functional consequences of presynaptic homeostatic plasticity at auditory nerve synapses. J. Neurosci. *40*, 6896–6909, JN-RM-1175-19.

Zürner, M., Mittelstaedt, T., Dieck, S.T., Becker, A., and Schoch, S. (2011). Analyses of the spatiotemporal expression and subcellular localization of liprin-α proteins. J. Comp. Neurol. *519*, 3019–3039.

## STAR★METHODS

### KEY RESOURCES TABLE

| REAGENT or RESOURCE | SOURCE | IDENTIFIER |
|---|---|---|
| Antibodies | | |
| Guinea pig anti-synapsin ½ | Synaptic System | Cat.# 106004<br>RRID:AB_1106784 |
| Rabbit anti-RIM1 | Synaptic System | Cat.# 143003<br>RRID:AB_887774 |
| Rabbit anti-RIM1 | Synaptic System | Cat.# 143023<br>RRID:AB_2177807 |
| Rabbit anti-ELKS | Synaptic System | Cat.# 140003<br>RRID:AB_887715 |
| Rabbit anti-RFP | Abcam | Cat.# Ab62341<br>RRID:AB_945213 |
| Mouse anti-bassoon | Enzo LifeScience | Cat.# SAP7F407<br>RRID:AB_10618753 |
| Rabbit RIM-BP2 | Synaptic System | Cat.# 316103<br>RRID:AB_2619739 |
| Mouse anti-SRPK2 | Santa Cruz | Cat.# Sc-136078<br>RRID:AB_2194850 |
| Mouse anti-PSD95 | Neuromab | Cat.# 75-028<br>RRID:AB_2292909 |
| Mouse anti- β-actin | Abcam | Cat.# Ab6276<br>RRID:AB_2223210 |
| Rabbit anti-synaptophysin | Abcam | Cat.# Ab52636<br>RRID:AB_882786 |
| Rabbit anti-liprin-α3 | Zürner et al. (2011) | N/A |
| Rabbit anti-Munc13 | Synaptic System | Cat.# 126102<br>RRID:AB_887734 |
| Mouse anti-Munc13 | Synaptic System | Cat.# 126111<br>RRID:AB_887735 |
| Mouse anti-Rab3 | Synaptic System | Cat.# 107011<br>RRID:AB_887768 |
| Mouse anti-HA | Covance | Cat.# 16B12 |
| Mouse anti-FLAG | Sigma-Aldrich | Cat.#F1804<br>RRID:AB_262044 |
| Goat anti-rabbit CF568 | Sigma-Aldrich | Cat.# SAB4600085 |
| Goat anti-mouse CF568 | Sigma-Aldrich | Cat.# SAB4600082 |
| Alexa Fluor® 647 Goat anti-mouse | Life Technologies | Cat.# A-21236<br>RRID:AB_141725 |
| Alexa Fluor® 647 Goat anti-guinea pig | Life Technologies | Cat.# A-21450<br>RRID:AB_141882 |
| Alexa Fluor® 647 Goat anti-rabbit | Life Technologies | Cat.# A-21244<br>RRID:AB_141663 |
| Alexa Fluor® 488 Goat anti-guinea pig | Life Technologies | Cat.# A-11073<br>RRID:AB_2534117 |
| Donkey anti-guinea pig Cy3 | Jackson ImmunoResearch | Cat.# 706-165-148<br>RRID:AB_2340460 |
| IRDye® goat anti-mouse 680RD | LI-COR Biosciences | Cat.# 926-68072<br>RRID:AB_10953628 |
| IRDye® goat anti-rabbit 800CW | LI-COR Biosciences | Cat.# 926-32211<br>RRID:AB_621843 |

(*Continued on next page*)

*Continued*

| REAGENT or RESOURCE | SOURCE | IDENTIFIER |
|---|---|---|
| **Bacterial and virus strains** | | |
| Stellar™ competent cells | Takara Bio | Cat.# ST0213 |
| MAX Efficiency™ Stbl2™ Competent Cells | ThermoFisher | Cat.# 10268019 |
| One Shot™ BL21(DE3) pLysE Chemically Competent E. coli | ThermoFisher | Cat.#C656503 |
| **Chemicals, peptides, and recombinant proteins** | | |
| Tetrodotoxin | Tocris | Cat.# 1078 |
| CNQX | Tocris | Cat.# 0190 |
| DL-AP5 | Tocris | Cat. # 0105 |
| β-Mercaptoethylamine hydrochloride (MEA) | Sigma-Aldrich | Cat. # 30070 |
| Catalase | Sigma-Aldrich | Cat. #C9322-1G |
| Glucose oxidase | Sigma-Aldrich | Cat. # 9180-250MG |
| CL114 | Logopharm | Cat.# CL114 |
| FM4-64 | Life Technologies | Cat.# T-3166 |
| SRPK2 | SignalChem | Cat. #S22-10G-10 |
| Myelin basic protein | Sigma-Aldrich | M1891-1MG |
| RIM1-S285 (QKQASRSRSEPPRER) | This paper | N/A |
| RIM1-S346 (RLEKGRSQDYSDR) | This paper | N/A |
| RIM1-S379 (IYQTRYRSDPNLAR) | This paper | N/A |
| RIM1-S514 (SMLRNDSLSSDQS) | This paper | N/A |
| RIM1-S742 (PSISVISPTSPGA) | This paper | N/A |
| RIM1-S991 (NVPLQRSLDEIHP) | This paper | N/A |
| RIM1-S1045 (RAKRGRSAESLHM) | This paper | N/A |
| RIM1-S1078 (PDTSLHSPERERH) | This paper | N/A |
| RM1-S1175 (VSRRSRSTSQLSQ) | This paper | N/A |
| RIM1-S1203 (VPVRSGSIEQASL) | This paper | N/A |
| RIM1-S1234 (TTGSGSSQELDHE) | This paper | N/A |
| RIM1-S1339 (RNDGSQSDTAVGT) | This paper | N/A |
| RIM1-S1600 (PLTRRASQSSLES) | This paper | N/A |
| RIM1-negative control (IVVRDMAVVRDMA) | This paper | N/A |
| MRFP | M. Geyer | N/A |
| TMT10plex Isobaric Label Reagent Set, 1 x 0.8 mg | Thermo Fisher | Cat. # 90110<br>Lot No. QK226224 |
| **Deposited data** | | |
| Raw mass spectrometry files and MaxQuant peptide-spectrum matching output files | PRIDE | PXD016636 |
| **Experimental models: Cell lines** | | |
| HEK293T for AAV production | Clontech | Cat. #: 632273 |
| HEK293T for lenti production | Clontech | Cat. #: 632180 |
| **Experimental models: Organisms/strains** | | |
| Mouse: C57Bl6/N-mice | Charles River | N/A |
| Mouse: Rims1$^{tm3Sud}$/J | Kaeser et al. (2011) | PRID:IMSR_JAX:015832 |
| Mouse: Rims2$^{tm1.1Sud}$/J | Kaeser et al. (2011) | PRID:IMSR_JAX:015833 |
| **Oligonucleotides** | | |
| shRNA against SRPK2 FW: gatcttcGCAGA GAGTGATTACACGTATCTCGA GATACGTGTAATCACTCTCTGCTTTTTggaaa | This paper | N/A |

(*Continued on next page*)

*Continued*

| REAGENT or RESOURCE | SOURCE | IDENTIFIER |
|---|---|---|
| shRNA against SRPK2 Rev: agcttttccAAAAA GCAGAGAGTGATTACACGT ATCTCGAGATACGTGTAATCACTCTCTGCga | This paper | N/A |
| **Recombinant DNA** | | |
| pCMV6-SRPK2 | ThermoFisher | Image clone-ID: 4507346 |
| AAV-CMV-HA-SRPK2 | This paper | N/A |
| AAV-CMV-RIM-N-Flag | This paper | N/A |
| AAV-CMV-RIM-C-Flag | This paper | N/A |
| pCAG-mGFP | Matsuda and Cepko (2007) | RRID:Addgene_14757 |
| AAV-Gap43-EGFP | This paper | N/A |
| AAV-Gap43-EGFP-SRPK2 | This paper | N/A |
| AAV-CMV-HA-SRPK2-DM | Liang et al. (2014) | N/A |
| AAV-CMV-HA-SRPK2-DSI | Liang et al. (2014) | N/A |
| AAV-CMV-HA-SRPK2DNSI | Liang et al. (2014) | N/A |
| pNCS-mNeonGreen (=mNeon) | Allele Biotechnology | Cat.# ABP-FP-MNEONSA |
| mRFP-N1 | Campbell et al. (2002) | Addgene #54635 |
| AAV-CMV-mNeon-RIM1-C2A | This paper | N/A |
| AAV-CMV-mNeon-RIM1-C2B | This paper | N/A |
| AAV-CMV-SRPK2-mRFP | This paper | N/A |
| rAAV-CMV-GFP-SRPK2 | This paper | N/A |
| rAAV-CMV-GFP-SRPK2-K108R | Vivarelli et al. (2013) | N/A |
| rAAV-CMV-mturquoise-SRPK2 | This paper | N/A |
| rAAV-U6-GFP | This paper | N/A |
| rAAV-U6-mturquoise | This paper | N/A |
| rAAV-U6-GFP-shSRPK2 | This paper | N/A |
| rAAV-U6-mturquoise-shSRPK2 | This paper | N/A |
| rAAV-synI-SF.iGluSnFR.A184V | Marvin et al. (2018) | N/A |
| rAAV-CBA-Cre | This paper | N/A |
| CMV-SyGCamp6f | L. Lagnado | N/A |
| rAAV-Syn-Synaptophysin-GCamp6 | This paper | N/A |
| pLVX-DsRed-Express2-N1 | Clontech | Cat.# 632560 |
| pLenti-Ef1α-GFP-RIM1α (*wt*RIM1) | This paper | N/A |
| pLenti-Ef1α-GFP-RIM1α (S346E) | This paper | N/A |
| pLenti-Ef1α-GFP-RIM1α (S443/447A) | This paper | N/A |
| pLenti-Ef1α-GFP-RIM1α (S514A) | This paper | N/A |
| pLenti-Ef1α-GFP-RIM1α (S745A) | This paper | N/A |
| pLenti-Ef1α-GFP-RIM1α (S745E) | This paper | N/A |
| pLenti-Ef1α-GFP-RIM1α (S895A) | This paper | N/A |
| pLenti-Ef1α-GFP-RIM1α (S991A) | This paper | N/A |
| pLenti-Ef1α-GFP-RIM1α (S991E) | This paper | N/A |
| pLenti-Ef1α-GFP-RIM1α (S1045A) | This paper | N/A |
| pLenti-Ef1α-GFP-RIM1α (S1045E) | This paper | N/A |
| pLenti-Ef1α-GFP-RIM1α (S1203E) | This paper | N/A |
| pMD2.G | Addgene | Cat. # 12259 |
| psPax2 | Addgene | 12260 |
| pGEX-RIM1-S285 | This paper | N/A |
| pGEX-RIM1-S346 | This paper | N/A |
| pGEX-RIM1-S379 | This paper | N/A |

(*Continued on next page*)

*Continued*

| REAGENT or RESOURCE | SOURCE | IDENTIFIER |
|---|---|---|
| pGEX-RIM1-S514 | This paper | N/A |
| pGEX-RIM1-S742 | This paper | N/A |
| pGEX-RIM1-S991 | This paper | N/A |
| pGEX-RIM1-S1045 | This paper | N/A |
| pGEX-RIM1-S1078 | This paper | N/A |
| pGEX-RIM1-S1175 | This paper | N/A |
| pGEX-RIM1-1203 | This paper | N/A |
| pGEX-RIM1-1234 | This paper | N/A |
| pGEX-RIM1-S1339 | This paper | N/A |
| pGEX-RIM1-S1600 | This paper | N/A |
| pGEX-RIM1-NC (negative control) | This paper | N/A |
| pGEX-RIM1-N (AA: 1-715) | This paper | N/A |
| pGEX-RIM1-C (AA: 735-1615) | This paper | N/A |
| pGEX-RIM1-Fragment 1 (AA: 1-507) | This paper | N/A |
| pGEX-RIM1-Fragment 2 (AA: 500-952) | This paper | N/A |
| pGEX-RIM1-Fragment 3 (AA: 755-1311) | This paper | N/A |
| pGEX-RIM1-Fragment 4 (AA: 1312-1615) | This paper | N/A |
| Software and algorithms | | |
| Igor Pro | WaveMetrics | https://www.wavemetrics.com/ |
| Mathematica | Wolfram Research | https://www.wolfram.com/mathematica/ |
| ImageJ | National Institutes of Healths | https.//imagej.nih.gov/ij/ |
| GraphPad Prism (Version 6.02) | GraphPad Software Company | https://www.graphpad.com/scientific-software/prism/ |
| NIS Elements | Nikon | https://www.microscope.healthcare.nikon.com/products/software |
| LAS AF | Leica | https://www.leica-microsystems.com/de/produkte/mikroskop-software/p/leica-las-x-ls/ |
| Odyssey Fc Imaging system and Image Studio Lite (v. 5.2) | Li-Cor Corporate Company | https://www.licor.com/bio/image-studio-lite/ |
| Imaris | Bitplane | https://imaris.oxinst.com/packages |
| EspINA Interactive Neuron Analyzer | Cajal Blue Brain Project | http://cajalbbp.es/espina/ |
| MatLab | MathWorks | https://de.mathworks.com/products/matlab.html |
| phosphoprocessR (Version 0.99.8) | Waardenberg AJ, 2017, Methods Mol Biol. doi: https://doi.org/10.1007/978-1-4939-6955-5_17 | https://github.com/awaardenberg/phosphoProcessR |
| R version 3.4.4 | NA | https://www.r-project.org/ |
| Mathematica Code for density maps (dSTORM analysis) | This paper | Zenodo: https://doi.org/10.5281/zenodo.6350182 |
| Limma (Version 3.36.5) | Bioconductor | N/A |

## RESOURCE AVAILABILITY

### Lead contact

Further information and requests for resources should be directed to and will be fulfilled by Susanne Schoch McGovern, at susanne.schoch@uni-bonn.de.

### Materials availability

There are no restrictions to the availability of generated plasmids and other generated material in this study and they may be requested from the corresponding author.

### Data and code availability

- The raw mass spectrometry datasets generated in this study are available via PRIDE: PXD016636, http://www.ebi.ac.uk/pride/archive/projects/PXD016636.
- All original code has been deposited at Zenodo: https://doi.org/10.5281/zenodo.6350182, and is publicly available as of the date of publication.
- Any additional information required to reanalyze the data reported in this paper is available from the lead contact upon request.

## EXPERIMENTAL MODEL AND SUBJECT DETAILS

### Animals

C57BL/6N-mice (Charles River, Sulzfeld, Germany) and conditional RIM1/2flox/flox mice (RIM1flox:RIM2flox: RIMS1$^{tm3Sud}$/J, RIMS2$^{tm1.1Sud}$/J, Jackson Lab) (Kaeser et al., 2011) of both sexes were used for all analyses (E16-18 for neuronal cultures, 2-3 months for all other analyses). Mice were housed under a 12 h light-dark-cycle (light-cycle 7AM/7PM), in a temperature (22 ± 2°C) and humidity (55 ± 10%) controlled environment with food/water *ad libitum*. All procedures were planned and performed in accordance with the guidelines of the University of Bonn Medical Center Animal-Care-Committee as well as the guidelines approved by the European Directive (2010/63/EU) on the protection of animals used for experimental purposes.

### Neuronal cell cultures

Mouse hippocampal and cortical neurons were prepared from embryonic mice (E16-18) as previously described (Zürner et al., 2011). In brief, hippocampi or cortices were dissected from the embryonic mice, washed several times with HBSS (Life Technologies) and subsequently digested with trypsin (Life Technologies) for 20 min at 37°C (0.025 g/mL, Life Technologies). After several washing steps with HBSS, the remaining DNA was digested with DNase I (0.001 g/mL, Roche). Cannulas were used to dissociate the tissue and the suspension was passed through a Nylon cell strainer (100 μm, BD Biosciences). Cells were seeded in a 12 or 24-well plate on glass coverslips coated with poly-D-lysine at a density of 25,000 cells per 24-well or 30,000 cells per 12-well. For proteomic analysis, cells were plated in a 6-well plate with 300,000 cells per well. All cells were cultured in basal medium eagle (BME, Life Technologies) supplemented with 0.5% glucose (Sigma-Aldrich), 1% fetal calf serum (FCS, Life Technologies), 2% B-27 and 0.5 mM L-glutamine (Life Technologies) or Neurobasal medium (Thermo Fisher). Cells were maintained at 37°C in 5% $CO_2$ until use. For transfection experiments, cultured neurons were transfected on DIV2-6 with 0.5–0.1 μg plasmid DNA using Lipofectamine2000 (Life Technologies) according to the manufacturer's instructions.

### HEK293T cells

HEK293T cells were cultured in Dulbecco's Modified Eagle Medium (DMEM, Life Technologies) supplemented with 5% (v/v) penicillin/streptomycin (Life Technologies) and 10% (v/v) FCS. For transfection, cells were seeded at a density of 1.5 x $10^6$ on 10 cm dishes. Four hours prior to transfection the medium was exchanged to Iscove's Modified Dulbecco's Medium (IMDM, Life Technologies) with 5% FCS. Calcium-phosphate transfection or Lipofectamine2000 were used to deliver 5 μg DNA (for GAP43 and GAP43-SRPK2 0.5 μg were used) plasmid to the cells. The medium was exchanged to DMEM 24 h after transfection. Cells were lysed 48 h after transfection or fixed for staining.

## METHOD DETAILS

### Antibodies

The following commercial primary and secondary antibodies were used in this study (IF = Immunofluorescence; IB = Immunoblot):

anti-Synapsin1/2 (IF: 1:3000, IB: 1:1000, Synaptic Systems 106,004), anti-RIM1 (IF: 1:1000, Synaptic Systems 143,003; IB: 1:1000, Synaptic System 143,023), anti-ELKS1/2 (IF/IB: 1:1000, Synaptic Systems 140,003), anti-bassoon (IF: 1:5000, Enzo LifeScience, SAP7F407), anti-RIM-BP2 (IF: 1:500, IB: 1:1000, Synaptic Systems 316,103), anti-SRPK2 (IF/IB: 1:100, SantaCruz, Sc-136078), anti-PSD-95 (IF: 1:200, Neuromab, 75-028), anti-β-actin (IB: 1:10,000, abcam ab6276), anti-synaptophysin (IB: 1:1000, abcam, ab52636), anti-Liprin-α3 (IB: 1:1000, Zürner et al., 2011), anti-Munc13 (IB: 1:500, Synaptic Systems 126,111 or IB: 1:500, Synaptic Systems 126,102), anti-rab3 (1:1000, Synaptic Systems 107,011), anti-RFP (IB: 1:1000, abcam ab62341), anti-Flag (IB: 1:1000, Sigma-Aldrich, 16B12).

The following fluorescent-conjugated secondary antibodies were used: goat-anti mouse/rabbit CF568 (IF: 1:200, Sigma-Aldrich, SAB4600085 (rabbit), SAB4600082 (mouse)), Alexa Fluor 647 goat anti-mouse (IF: 1:200, Life Technologies, A21236), Alexa Fluor 647 goat anti-rabbit (IF: 1:200, Life Technologies, A21244), Alexa Fluor 647 goat anti-guinea pig (IF: 1:200, Life Technologies, A21450), Alexa Fluor 488 goat anti-guinea pig (IF: 1:200, Life Technologies, A11073), donkey anti-guinea pig Cy3 (IF: 1:400, Jackson ImmunoResearch, 926-68,022). For immunoblots IRDye goat anti-mouse 680RD or anti-rabbit 800CW (IB: 1:20,000; LI-COR) were used as secondary antibodies.

### Viral vector production

Recombinant AAV1/2 particles were generated by triple transfection of HEK293T cells as described previously (Loo et al., 2012). In brief, calcium phosphate transfection of the adeno-associated virus (AAV) plasmid of interest, helper plasmids encoding rep and

cap genes (pRV1 and pH21) and adenoviral helper pFΔ6 was performed. Medium was exchanged to DMEM 24 h after transfection and viral particles were harvested 48-72 h later. To prepare crude viral extracts, cells were resuspended in 1 mL of DMEM (supplemented with 5% penicillin/streptomycin and 10% FCS) and the cell suspension was frozen at −80°C. After three freeze/thaw cycles, cells were centrifuged and the supernatant was kept at 4°C. To generate purified rAAV virus cell pellets were lysed in lysis buffer (0.5% sodium deoxycholate (Sigma-Aldrich) with 50 units/ml Benzonase (Sigma-Aldrich)). HiTrapTM heparin columns (GE Healthcare) were used to purify rAAV viral particles from the cell lysate. rAAV viral particles were concentrated using Amicon Ultra Centrifugal Filters (Millipore) to a final stock volume of 500 μL. Purity of viruses was validated using Coomassie blue staining of SDS-polyacrylamide gels. Primary neurons were infected with 5 μL of crude viral extracts per 24-well (rAAV-SRPK2-kDead-GFP). For purified AAV viruses containing ~$10^8$ transducing units either 1 - 2 μL per 24-well or 5 μL per 6-well were used. All primary neurons were infected 2-6 days after plating.

Lentiviruses were produced using a second-generation packaging system, as previously described (Loo et al., 2019). In brief, 3 x $10^6$ HEK293T cells (Clontech) were seeded on a 10 cm cell culture dish and transfected after 24 h with GenJet transfection reagent (Signagen). Per dish 7.5 μg packaging plasmid (psPax2, Addgene), 5 μg VSV-G expressing envelope plasmid (pMD2.G, Addgene) and 4 μg plasmid of interest (e.g. pLenti-Ef1α-GFP-RIM1α) were used. After 12 h, transfection medium was replaced with DMEM containing Glutamax (Invitrogen) supplemented with 10% FBS. Transfected cells were incubated for 72 h to allow formation of viral vectors. Thereafter, the supernatant was filtered through 0.45 μm PVDF membrane filters (GE Healthcare) to remove cell debris and other aggregates. To purify the virus, the filtered supernatant was layered on top of OptiPrep density gradient medium (Sigma-Aldrich) and centrifuged at 24,000 rpm for 2 h at 4°C using an SW-Ti32 swinging bucket (Beckman Coulter). The upper layer was discarded. The Opti-Prep-Layer, with the viral particles at its upper boundary, was mixed with TBS-5 buffer (containing in mM: 50 Tris-HCl, 130 NaCl, 10 KCl, 5 $MgCl_2$). Viral particles were pelleted by centrifugation (24,000 rpm for 2 h at 4°C) and resuspended in TBS-5 buffer. Lentiviruses were stored at −80°C until use. Primary neurons cultured on coverslips in 24-well plates were transduced with 1 - 2 μL of lentiviral suspension per well at DIV2-6.

## Constructs

The following plasmids were kindly provided by J Ngo (SRPK2-DM, SRPK2-ΔSI and SRPK2-ΔNSI; Liang et al., 2014), SM Barabino (Kinase dead version of SRPK2 (CMV-SRPK2-K108R), Vivarelli et al., 2013), L. Looger (rAAV-SF.iGluSnFR.A184V, Marvin et al., 2018).

The plasmid pCMV6-SRPK2 (Image clone-ID4507346) was used to amplify the cDNA coding for SRPK2 (mouse). The SRPK2 cDNA was cloned into a pCMV-MCS vector (Stratagene/Agilent) using XbaI and SalI restriction enzymes, while the sequence of the HA tag was inserted with ClaI and XbaI. To generate the shSRPK2 plasmid, Pam-U6 was digested with BglII and HindIII and ligated with the oligonucleotide containing the shRNA against SRPK2 (sequence of shRNA listed in Key resources table).

To generate the CMV-GAP43-EGFP and CMV-GAP43-EGFP-SRPK2 plasmids, the sequence of GAP43-EGFP was amplified by PCR from the pCAG-mGFP plasmid (Addgene) as template. The GAP43-EGFP fragment was cloned with ClaI and XbaI into the pCMV-MCS vector. SRPK2 was amplified by PCR from pCMV6-SRPK2 and cloned with XbaI and SalI.

RIM1-N (1-663aa) and RIM1-C (685-1615aa) containing the Zn-finger-PDZ- and C2A-C2B-domains and surrounding linker regions of RIM1α were generated by PCR using rat RIM1α as template. The RIM1-N domain of RIM1α was cloned with EcoRI and AvrII and the RIM1-C domain of RIM1α with EcoRI and SalI into the pCMV-MCS vector (Stratagene/Agilent). A Strep-FLAG tag sequence was introduced in the C-terminal position of RIM1-N using AvrII-HindIII or SalI-HindIII in the case of RIM1-C.

For GST pull-down assays full-length SRPK2 was cloned with AvrII and SalI into the pGEX vector. The C2A domain of RIM1α was inserted using EcoRI and XhoI. Other RIM1 fragments were cloned into the pGEX vector with XbaI. Oligonucleotides of RIM1 were inserted into pGEX using EcoRI and SalI.

To generate pLenti-EF1α-GFP-RIM1α plasmid, the multiple cloning site in pLVX-DsRed-Express2-N1 was exchanged to yield restriction sites for EcoRI, NsiI, AvrII, BstZ17I and NdeI and Ef1α-dsRed was replaced by Ef1α-GFP using restriction sites ClaI and EcoRI. RIM1α was amplified from rat cDNA in four fragments with primers containing the above-mentioned restriction sites. Point mutations of phosphorylation sites were introduced to pLenti-Ef1α-GFP-RIM1α using QuickChange Lightning Site-Directed Mutagenesis Kit (Agilent Technologies) according to the manufacturer's instructions.

mNeonGreen was bought from Allele Biotechnology (USA) and mRFP from Addgene (Campbell et al., 2002). mNeon-RIM1-C2A (mouse), mNeon-RIM1-C2B (mouse) and SRPK2(mouse)-mRFP constructs were generated by in-fusion cloning (Clontech). Primers were designed to introduce a flexible SRG4SG4S linker between the fused proteins. Amplified fragments were cloned into the AAV-CMV-MCS (Stratagene, USA) plasmid via XbaI/HindIII restriction sites. All the above generated plasmids were verified by sequencing.

## Subcellular fractionation

Subcellular fractionation was performed from adult mouse brains. Whole brains were homogenized in a buffer containing 0.32 M sucrose (Roth) and 4 mM HEPES with pH set to 7.4, supplemented with proteinase inhibitor. For homogenization a Teflon-glass homogenizer was used and 12 strokes at 900 rpm were applied. Homogenates were centrifuged for 15 min at 3,000 g. Supernatant 1 was centrifuged for 25 min at 14,000 rpm. Crude synaptosomes (Pellet 2, P2) were lysed for 30 min in 1% Triton with proteinase inhibitor and subsequently centrifuged for 30 min at 50,000 g. Pellet 3 was resuspended in 1% Triton X-100 and again centrifuged for

30 min at 50,000 g. Supernatant 4 (S4) was separated from pellet 4, which was resuspended in 1% Triton X-100. Protein concentration was measured with a NanoDrop (Thermo Scientific).

### Protein purification from HEK293T cells

Plasmids coding for the zinc-finger/PDZ- (RIM-N) and C2-domains (RIM-C) of RIM1α, SRPK2-HA, SRPK2-GFP, SRPK2-kinase-dead-GFP were used to transfect HEK293T cells. Cells were lysed for 1 h at 4°C in ice-cold lysis buffer (containing in mM: 50 HEPES (Roth), 150 NaCl (Roth), 1% Triton X-100 (Sigma-Aldrich) supplemented with Complete Protease Inhibitor Cocktail Tablets (Roche), pH 7.4) and spun at 14,000 rpm for 10 min at 4°C. The supernatant was incubated for 1 h with magnetic beads (FLAG-M2, Sigma-Aldrich or GFP-Trap_M, ChromoTek) on a rotator for immunoprecipitation. The beads were separated by using a magnetic rack and washed twice in low salt wash buffer (50 mM HEPES pH7.4, 100 mM NaCl, 0.5% Triton X-100 (w/v)), two times in high salt wash buffer (50 mM HEPES pH7.4, 500 mM NaCl, 0.5% Triton X-100) and again twice in low salt wash buffer.

### Fluorescent protein lysate preparation from HEK293T cells

48 h post-transfection cells were lysed in 500 μL of lysis buffer, incubated for 1 h at 4°C and centrifuged at 14,000 rpm for 10 min at 4°C. Supernatant (stock lysate) containing the fluorescent protein of interest, was used for further experiments. For experiments lysates with different fluorescent proteins were mixed at different ratios in a total volume of 300 μL: mNeon lysates were diluted 1:20 from the stock lysate; mRFP lysates were diluted 1:0.05, 1:0.5*, 1:1, 1:2*, 1:3*, 1:4*, 1:5, 1:7*, 1:19 (* were not tested in all experiments). To estimate the absolute concentration of SRPK2-mRFP in the HEK293T lysate, immunoblots were performed and the SRPK2-mRFP bands were compared against bands of purified mRFP with a known concentration (purified mRFP was kindly provided by Matthias Geyer, Institute of Structural Biology, Bonn, Germany).

### Subcellular fractionation

Synaptosomes were prepared from transduced cortical neurons. Neurons were scraped in homogenization buffer (0.32 M sucrose, 50 mM EDTA, 2 mM HEPES pH7.4, proteinase inhibitor (1:1000) and filtered through a pre-wet 5 μm membrane filter (Millipore). Lysates were centrifuged at 3,500 rpm for 15 min. The pellets were resuspended in lysis buffer (10 mM HEPES, 150 mM NaCl, pH 7.5, 1% NP40 (Sigma-Aldrich), proteinase inhibitor (1:1000)) for 1 h at 4°C and subsequently centrifuged for 10 min at 14,000 rpm.

### Immunoblotting

Cortical or hippocampal neurons were transduced at DIV2-6 with rAAV-U6-GFP, -shSRPK2-GFP, -SRPK2-GFP and lysed at DIV14-16. For whole brain homogenates, brains were dissected at the indicated time points (P0-P30) and immediately frozen in liquid nitrogen. For homogenization, 0.02 mL/mg PBS with proteinase inhibitor (1:1000) was added and brains were homogenized using a RotorStator. Homogenates were sonicated before being separated by SDS-PAGE.

Proteins were separated by SDS-PAGE and transferred to PVDF or nitrocellulose membranes (Sigma-Aldrich). The membrane was blocked with 5% (w/v) milk powder (Roth) in 1x PBS-Tween-20 (0.1% (v/v), Sigma-Aldrich) for 1 h at room temperature. Primary and secondary antibodies were diluted in 1% milk powder solved in 1x PBS-Tween-20. Membranes were incubated with primary antibodies for 2 h and secondary antibodies for 1 h at RT and extensively washed after each incubation step.

### Crude synaptosome preparation and binding assay with subsequent MS analysis

For crude synaptosomes preparation 6-8 weeks C57BL/6N mice were used. After the removal of cerebellum, cortical hemispheres were homogenized in ice-cold homogenization buffer (0.32 M sucrose, 50 mM EDTA, pH 7.4) supplemented with proteinase inhibitors (Roche) in a Teflon-glass homogenizer, applying seven strokes at a rotation of 900rpm. The homogenate was spun at 3,000 g for 15 min at 4°C. The pellet (P1 = nuclear fraction) was discarded and the supernatant (S1 = crude synaptosomal fraction) centrifuged at 14,000 rpm for 25 min at 4°C. The resulted pellet (P2) containing the crude synaptosomes was pre-equilibrated in Krebs-Henseleit-HEPES buffer (118 mM NaCl, 3.5 mM KCl, 1.25 mM $CaCl_2$, 1.2 mM $MgSO_4$, 1.2 mM $KH_2PO_4$, 25 mM $NaHCO_3$, 11.5 mM glucose and 5 mM HEPES-NaOH, pH 7.4) for 10 min at 37°C. Thereafter, crude synaptosomes were treated for 15 min at 37°C with either methanol, stauroporine (1μM, Sigma) or phosSTOP (1x, Roche). Synaptosomal proteins were extracted by lyses for 1 h at 4°C in CL114 detergent (Logopharm). After centrifugation (14,000 rpm for 20 min at 4°C), the clear supernatant (4-5μg) was incubated for 3-4 h with the purified ZF-PDZ domain or C2A-C2B domain of RIM1α. Magnetic beads were separated by using a magnetic rack and washed several times in CL114 dilution buffer. Bound complexes were eluted from the beads by boiling at 95°C in 1x loading buffer (Life Technologies) and resolved in a pre-cast NuPAGE4-12% Bis-Tris gel (Life Technologies). Bands were visualized by Coomassie Colloidal Blue (Carl Roth).

Bands of interest were excised from the gel with a scalpel, destained according to the manufacturer's instruction (Sigma Protocol IGD profile kit) and dried in a vacuum concentrator for 30-40 min at RT. Proteins were reduced with 20 mM DTT (prepared in 100 mM ammonium hydrogencarbonate) at 55°C for 30 min and the generated thiol groups were alkylated in the presence of 40 mM iodoacetamide (prepared in 100 mM ammonium hydrogencarbonate) for 30 min at RT and protected from light. After these treatments the gel pieces were completely dried in the vacuum concentrator and digested at 37°C overnight with 0.4 μg of trypsin. Sample preparation and the measurements were performed in the mass spectrometry facility of the Institute of Biochemistry and Molecular Biology, Bonn.

### Immunoprecipitation and GST-pull down

Various SRPK2 variants were expressed in HEK293T cells and immunoprecipitated using HA- (Life technologies) or GFP- (ChromoTek) magnetic beads, respectively. Crude synaptosomes from mouse brains were prepared as described above to evaluate the binding of SPRK2 to synaptic proteins. After lysis of synaptosomes (P2) with CL114 lysis buffer (Logopharm) for 1 h at 4°C, synaptosomes were centrifuged at 14,000 rpm for 20 min. The supernatant was incubated with the immunoprecipitated SRPK2 variants from HEK293T cells for 4 h. Subsequently, SRPK2 bound to beads was washed five times with CL114 dilution buffer (Logopharm). Samples were analyzed by SDS-PAGE and immunoblot analysis.

### *In vitro* phosphorylation

Expression of rat RIM1-peptides fused to glutathione S-transferase (GST) was induced in BL21DE3 bacteria by addition of 0.1 mM IPTG (β-D-1-thiogalactopyranoside, Roth). GST-fusion proteins were purified using glutathione-agarose beads (Sigma-Aldrich). GST-fusion peptides and myelin basic protein (MBP, bovine, Sigma) were incubated with 500 ng SRPK2 for 30 min at 37°C in kinase reaction buffer III (SignalChem, 200 mM Tris-HCl, pH 7.4, 100 mM $MgCl_2$, 0.5 mg/mL BSA, 0.25 mM DTT) and 1 mM ATP (SignalChem).

For radiometric *in vitro* phosphorylation, 3 μCi [$^{32}$P]-γ-ATP (PerkinElmer) was added per reaction and the reaction was stopped with 10 μL 4 x SDS-PP (200 mM Tris-HCl (Roth) (pH 6.8), 400 mM DTT (Thermo Fisher), 8% SDS (Roth), 0.4% bromophenol blue (Sigma-Aldrich), 40% glycerol (Invitrogen)). Reaction samples were transferred on a nitrocellulose membrane (0.45 μm pore size, GE Healthcare), which was washed 3 times with 5 mL 0.75% phosphoric acid (v/v) for 5 min. Radioactivity was counted in a Beckman Scintillation Counter (Beckman Coulter) for 1 min.

For *in vitro* phosphorylation followed by mass spectrometry analysis, beads were spun down and supernatant was removed. Beads were washed with wash solution (50 mM HEPES, pH 8.4) three times. After removal of washing solution, beads were resuspended in 40 μL reduction buffer (10 mM tris(2-carboxyethyl) phosphine hydrochloride (TCEP, Sigma-Aldrich), 50 mM HEPES pH 8.4) and incubated for 10 min at 85°C, while shaking at 600 rpm. Samples were returned to room temperature and iodoacetamide (Sigma-Aldrich) was added to a final concentration of 20 mM. Samples were incubated 30 min at room temperature in the dark. Afterward, 40 μL of TCEP was added to quench the alkylation. To digest proteins, trypsin (Sigma-Aldrich) was added to obtain a 1:20 ratio of trypsin:protein and samples were incubated at 37°C for 4 h. To achieve a better digestion, the same amount of trypsin was added a second time and samples were again incubated at 37°C for 4 h. To collect trypsinized peptides, beads were spun down and supernatant was collected. Beads were washed once with washing solution and supernatant was collected. Pooled supernatants were frozen on dry ice and subsequently lyophilized.

### Mass spectrometry of primary neurons

Mouse cortical neurons were transduced at DIV2-6 with rAAV U6-GFP, shSRPK2-GFP, SRPK2-GFP and lysed at DIV14-16 (2% SDS, 50 mM Tris/HCl pH 7.4, 2 mM EGTA (Roth), 2 mM EDTA (Roth), Complete Protease Inhibitor Cocktail, 2 mM PMSF (Sigma-Aldrich), 5 mM NaF (Sigma-Aldrich), 2 mM beta-glycerophosphate (Sigma-Aldrich), Phosphatase inhibitor Cocktail 2 (1:1000), PhosSTOP (Roche). Lysed cells were frozen on dry ice. Lysates were heated at 85°C for 10 min and afterward sonicated at maximum intensity three times for 10 s. Samples were refrozen on dry ice before being lyophilized.

To each sample 100 μL of water containing 10 mM tris(2-carboxyethyl) phosphine tris(2-carboxyethyl) phosphine was added. The samples were heated at 85°C for 10 min. Iodoacetamide was added to 20 mM and samples were incubated at 22°C for 30 min. Samples were precipitated by the chloroform-methanol-water method (Wessel and Flügge, 1984) and air dried at 37°C for 1 h. Samples were dissolved in 24 μL 7.8 M Urea with 50 mM HEPES and 4 μg of lysyl endopeptidase (Fujifilm/Wako, Japan) at pH 8.0 (adjusted with NaOH) and heated at 25°C for 8 h. Samples were diluted to 192 μL in HEPES/NaOH pH 8.0 and 4 μg of trypsin was added. The samples were incubated at 37°C for 4 h.

The amount of peptide in each sample was measured using the absorption of 280 nm light (Implen Nanophotometer, Labgear, Australia). Aliquots containing 100 μg of peptide were labeled with tandem mass tag (TMT) 10-plex reagents (Thermo Fisher Scientific), according to the manufacturer's instructions. There were two separate TMT10plex schemes: (i) five control samples (U6-GFP) were compared to five overexpression (SRPK2-GFP) samples and (ii) five control samples (U6-GFP) were compared to five knockdown samples (shSRPK2-GFP). The two sets of 10 tagged samples were separately combined to produce two 10-plex sample mixtures. These were acidified with formic acid. The volume was reduced by vacuum concentration and then made up in 1 mL of water with 0.1% trifluoracetic acid. The two samples were each desalted using a Sep-Pak tC18 3cc Vac Cartridge (200 mg sorbent, Waters).

The sample's eluate volume was reduced and then made up in a solution of 1 M glycolic acid, 5% trifluoracetic acid and 80% acetonitrile and applied to the "TiSH" method of phosphopeptide enrichment and hydrophilic interaction chromatography fractionation as described in detail previously (Engholm-Keller et al., 2019). This method first separates multi-site phosphopeptide from mono-phosphorylated peptides and then fractionates the mono-phosphopeptides. The hydrophilic interaction chromatography used a 5-μm TSKGel Amide 80 resin (Tosoh, Japan) column and was performed as described previously (Engholm-Keller et al., 2019).

The peptides from each hydrophilic interaction chromatography fraction and the multi-phosphorylated peptides were resolved by reversed phase chromatography on a 300 × 0.075 mm column packed with ReproSil Pur C18 AQ 1.9 μm resin (Dr Maisch, Germany) using an Ultimate 3000 RSLC nano system (Thermo Scientific, Germany). The chromatography buffer A was 0.1% formic acid in

water and buffer B was 0.1% formic acid, 90% acetonitrile and 9.99% water and the flow rate was 250 nL/min. The gradient was from 5% to 25% buffer B in 69 min, then to 35% buffer B in 8 min and to 99% buffer B in 3 min The column temperature was held at 50°C by a column oven (PRSO-V1, Sonation lab solutions, Germany). Peptides were detected by tandem mass spectrometry using a Q Exactive Plus hybrid quadrupole-orbitrap mass spectrometer. The Nanospray Flex ion source (Thermo Scientific, Germany) spray operated at 2.3 kV. The capillary temperature was 250°C and the S lens radio frequency level was 60. The MS scan was from m/z 375 to 1500 at a resolution of 70,000 full width at half maximum with an automatic gain control target of 1,000,000 counts for a maximum ion time of 100 ms. For each MS scan, up to 11 of the most intense ions above a threshold of 46,000 counts were selected for an MS/MS scan. MS/MS scans were at a resolution of 35,000 full width at half maximum for a maximum ion time of 120 ms and automatic gain control target of 20,000 counts. The isolation window was 1.2 units of the m/z scale, the fixed first mass was set at m/z 120 and the normalized collision energy was 34. Peptides with charge state <2 + or >8 + or with unassigned charge were excluded. Dynamic exclusion of previously scanned peptides was for 20 s.

An estimated 2 μg of the non-titanium dioxide binding (non-phosphorylated) peptides of each 10-plex sample mixture was also analyzed by LC-MS/MS. The settings were the same as for the phosphopeptides except for the following: The gradient was from 5% to 28% buffer B for 126 min, then to 35% buffer B in 10 min and to 99% buffer B in 3 min. Up to 12 of the most intense ions were selected for MS/MS above a threshold of 50,000 counts for a maximum ion time of 110 ms. Dynamic exclusion of previously scanned peptides was for 30 s.

The raw LC-MS/MS data were processed with MaxQuant v1.5.8.3 {Tyanova, 2016, 27,809,316} using the following settings: The fasta file was the Mus musculus reference proteome downloaded from UniProtKB on July 18, 2017 and containing 60,205 entries including protein isoforms. The reference proteome was combined with the default contaminants file and a reversed sequence database was used to assess the false discovery rate. Protease specificity was Trypsin/P with up to 3 missed cleavages. Carbamidomethyl (C) was a fixed modification and the TMT10plex reagents were designated isobaric labels. Deamidation (N and Q), oxidation (M), acetylation (protein N-terminus) and phosphorylation (S, T and Y) were variable modifications. A maximum of 5 modifications per peptide was allowed. The minimum score for modified peptides was 40. The minimum peptide length was 6 and maximum peptide mass was 7,000 Da. The peptide spectrum match, protein, and modification site false discovery rate was 1%. A dependent peptide search was performed with a 1% false discovery rate. Modified peptides and their counterpart non-modified peptides were excluded from protein quantification. A second peptide search was enabled. The tolerance for MS and MS/MS spectra was 4.5 ppm and 20 ppm, respectively. All other settings were left as the default within MaxQuant v1.5.8.3.

### Mass spectrometry of *in vitro* phosphorylated RIM1

The lyophilized peptide in each sample was desalted using a StageTip {Rappsilber, 2007, 17,703,201}. The samples were analyzed by LC-MS/MS using the same equipment as for mass spectrometry of neuronal samples. The settings were the same as for the neuronal phosphopeptides except for the following differences. The gradient was from 5% to 32% buffer B in 34 min, then to 99% buffer B in 2 min. Up to 12 of the most intense ions were selected for MS/MS above a threshold of 55,000 counts for a maximum ion time of 110 ms. The isolation window was 1.4 units of the m/z scale. The first fixed mass was at m/z 140. The normalized collision energy was 30. Dynamic exclusion of previously scanned peptides was for 25 s.

The MaxQuant processing was the same as the neuronal samples except for the following differences. The fasta file was the Rattus norvegicus reference proteome downloaded from UniProtKB on Feb 5, 2018, containing 29,975 entries of canonical protein isoforms. Match between runs was enabled with a matching time window of 0.7 min and alignment time window of 20 min. Maximum peptide mass was 5000 Da. No isobaric masses were enabled, as quantification was done using the intensity of the phosphopeptides in the MS scan.

### Immunohistochemistry of primary neurons

Hippocampal and cortical neurons were transduced or transfected at DIV2-6 with rAAV-U6-GFP, shSRPK2-GFP, SRPK2-GFP and fixed at DIV14-16 with 4% paraformaldehyde (PFA; 10 min). Neurons were incubated with 1 μM tetrodotoxin (TTX, Tocris) for 48 h prior to fixation to induce presynaptic homeostatic plasticity and subsequently fixed with 4% PFA.

After several washing steps with PBS (30 min), neurons were permeabilized with 0.3% Triton X-100 in PBS for 10 min and were blocked for 1 h in PBS with 10% normal goat serum (NGS, Thermo Fisher), 1% BSA (Roth) and 0.1% Triton X-100. Primary antibodies were incubated overnight at 4°C with the dilutions mentioned above. Coverslips with cells were mounted using Mowiol 4-88 (Roth).

### Immunohistochemistry of HEK293T cells

HEK293T cells were fixed in 4% PFA 24-48 h after transfection. Briefly, cells were permeabilized with 0.3% Triton X-100, blocked 1 h at room temperature and incubated with anti-RIM1/2 antibody (BD Bioscience, 1:200) overnight in blocking solution (1% BSA, 10% NGS, 0.1% Triton X-100 in PBS). On the next day, HEK293T cells were washed with PBS and incubated for 30 min with secondary antibodies and DAPI. After washing off the secondary antibodies, the coverslips were mounted on slides with Mowiol 4-88 and dried at room temperature overnight.

### Confocal imaging and analysis

Cells that were stained with immunocytochemistry were imaged using a laser-scanning microscope (Nikon Ti Eclipse with A1 confocal controller) with a Plan APO IR 60x WI objective (NA 1.27) and the NIS-Elements 4.0 (Nikon), if not stated differently.

Images for synapse analysis were captured with the confocal microscope and synapses were defined using a 20% intensity threshold of the synapsin staining. Synapsin staining was segmented and synapse area was set between 0.06 $\mu m^2$ - 0.85 $\mu m^2$. The fluorescence intensity of synaptic AZ proteins was normalized to fluorescent beads (InSpeckRed beads 0.1%, ThermoFisher). For each biological replicate, three technical replicates were imaged and averaged.

For analysis of the localization and amount of RIM1$\alpha$ mutants in the synapse, GFP-RIM1$\alpha$ constructs were transduced to neurons as above and GFP fluorescence was imaged at the confocal microscope as described. Images were thresholded and circular 1 $\mu m^2$ ROIs were placed on remaining fluorescence spots. The generated ROI set was used to measure the absolute mean fluorescence in the synaptic structures from the background subtracted images. Values were averaged per experiment and normalized to the control condition (wt RIM1$\alpha$ fused to GFP) from the same replicate.

### Direct stochastic optical reconstruction microscopy (dSTORM)

dSTORM imaging was performed on a Leica SR GSD 3D microscope (Leica Microsystems) with a 160x immersion oil objective (NA 1.47). The setup was equipped with 405- (30 mW), 488- (300 mW), 532- (500 mW) and 642-nm (500 mW) lasers. Excitation light was reflected to the sample via a quad band emission filter. dSTORM video sequence was imaged with a sCMOS camera (pco.edge4.2, PCO). To minimize stage drift, the microscope contained a suppressed motion (SuMo) stage.

Transfected cortical neurons were stained as described above. Labeled cells were imaged in GLOXY STORM imaging buffer (50 mM $\beta$-mercaptoethylamine hydrochloride (MEA), 10% (v/v) of a 250 g/L solution of glucose, 0.5 mg/mL glucose oxidase, 40 mg/mL catalase in PBS, pH 7.6), Nahidiazar et al., 2016 (PMID: 27391487)). Coverslips were mounted on depression slides and sealed with Twinsil silicone glue (Picodent). Before dSTORM acquisition, overview images were acquired in the laser widefield mode with 10% laser power for 488- and 532-nm lasers and 5% laser power for 642-nm laser with 500 ms exposure time each. dSTORM imaging with the 642-nm laser started after 20 s of pumping the fluorescent molecules to the dark state (50% laser power). For acquisition of RIM1, 30% laser power was used and 150,000 frames at 500 Hz were acquired. The detection threshold for stochastically occurring blink events was set to 8 photons/pixel for RIM1 in the Leica image acquisition software (LAS AF Version 1.9.0). The respective threshold was chosen such that unspecific blink events were avoided and only specific events were included in the dSTORM image reconstruction. Therefore, detected blink events in the raw image stack were fitted to a Gaussian. Blink events within a maximum xy distance of 70 nm from the first detected blink event with a maximum appearance of 10 frames were merged and treated as one molecule localization. 2D density histograms were rendered based on molecule coordinates and localization precisions with a pixel size of 20 nm.

### Electron microscopy

Hippocampal neurons were transduced at DIV2-6 with rAAV-U6-GFP, -shSRPK2-GFP, -SRPK2-GFP and fixed at DIV14-16 for 15 min with 4% PFA, 2.5% glutaraldehyde (AppliChem) and 2 mM $CaCl_2$ (VWR) dissolved in 0.01 M PBS. After, neurons were post-fixed with 1% $OsO_4$ (Science Services) and 0.8% K-ferricyanide (Roth) in 0.1 M cacodylate buffer (Roth) for 2 h. Neurons were dehydrated with an ascending ethanol (VWR) series, including 0.5% uranyl acetate (Science Services) in 70% ethanol, followed by 15 min propylene oxide incubation. Next, the neurons were infiltrated with epon (Sigma-Aldrich) and embedded in Epon at 60°C for 24 h. Coverslips were removed by dipping the embedded neurons in liquid nitrogen.

Three-dimensional (3D) image stacks were obtained with a focused ion beam - scanning electron microscope (FIB-SEM; Helios G4 CX, ThermoFisher). 5 nm thick slices were milled and images were acquired with 3 × 3 nm pixel size with the in-column detector at 2 kV and 0.34 nA.

### Two-photon fluorescence lifetime imaging microscopy (FLIM)

2-photon FLIM was performed using time-correlated single photon counting (TCSPC) at a Scientifica SliceScope 2-photon microscope system equipped with a Ti:sapphire laser (Coherent). mNeon was excited at 900 nm wavelength and 80 mHz frequency and the fluorescence was collected via a 20x objective using a custom-made filter cube with 525/50 nm (excitation) and 605/70 nm (amission) filters and a 560 nm beamsplitter. mNeon fluorescence was collected and correlated by Simple-Tau SPC-150 TCSPC module and Spcm64 software (Becker&Hickl, Germany). Photons were distributed in 256 time channels.

### FM4-64 styryl dye imaging experiments

Experiments were carried out at DIV13-21. All FM4-64 experiments were performed in imaging buffer (150 mM NaCl, 4 mM KCl, 2 mM $MgCl_2$, 2 mM $CaCl_2$, 10 mM D-glucose, 10 mM HEPES), supplemented with 10 $\mu$M CNQX (6-cyano-7-nitroquinoxaline-2,3-dione, Tocris) and 50 $\mu$M DL-AP5 (Tocris) to block ionotropic glutamate receptors and to suppress recurrent network activity. Recording solution was constantly perfused into the experimental chamber at 1 mL/min.

Cells were stimulated by electrical fields generated from bipolar platinum/iridium electrodes (two rods of 2 × 5 × 1 mm) in the presence of 10 $\mu$M FM4-64 to load the dye in recycling synaptic vesicles (90 s, 10 Hz, 20 mA, platinum/iridium electrodes). Following this loading procedure, extracellular dye was washed out for 8-9 min before image acquisition was started.

Images were acquired with an EM-CCD camera (Hamamatsu ImagEM X1) at 0.2 Hz acquisition rate with 20 ms exposure time. The camera was attached to an inverted microscope (Nikon T1 Eclipse) using a triggered, stabilized LED light source (Cairn OptoLED with 550 nm excitation wavelength and 550/49 excitation filter and 594 nm LP emission filter). Cells were imaged through a coverslip with

high numerical aperture objective (Zeiss, 63x, 1.4 numerical aperture, oil). Fluorescence baseline level with unstimulated loss of dye was monitored for 2 min before synaptic vesicle and FM4-64 release was provoked by electrical stimulation (5 Hz, 80 mA). After continuously stimulating for 5 min to quantify vesicle release rate a final round of high-frequency stimulation was applied to release all remaining dye-loaded vesicles (5 × 100 Hz for 1 s with 10 s rest in between). The remaining weak fluorescence was defined as background labeling.

### iGluSnFR experiments

iGluSnFR experiments were performed with the same microscope and stimulation setup as FM experiments using the same stimulation electrodes. All iGluSnFR experiments were carried out in imaging buffer as FM experiments. The single synapse analysis of iGluSnFr data is greatly facilitated when the density of activated synapses is low. For this reason, the adjustment of stimulation intensity was performed for each coverslip to minimize the number of activated synapses. Stimulation intensity was lowered until no optical responses were observed. Intensity was then gradually increased until responses just re-appeared and kept at this level to obtain the smallest fraction of activated axons possible (polysynaptic activation was avoided by CNQX and APV in the imaging buffer). Due to extensive arborization of axons of cultured neurons and the many synapses they form, this stimulation setting (mostly 20-40 mA) typically still yielded several hundred activated synapses per visual field. To induce presynaptic homeostatic plasticity, neurons were incubated with 1 μM TTX for 48 h. Prior to stimulation, TTX was washed out for 10 min using the imaging buffer. For experiments in high calcium concentration neurons were imaged in the described imaging buffer and afterward perfused with high $Ca^{2+}$ buffer (150 mM NaCl, 4 mM KCl, 0.5 mM $MgCl_2$, 4 mM $CaCl_2$, 10 mM D-glucose, 10 mM HEPES, pH set to 7.4, supplemented with CNQX and DL-AP5) for 5-10 min and then imaged again under the same imaging settings.

For iGluSnFR imaging a standard GFP filter cube (Emission: 470/40, Excitation: 525/50, beam splitter: 495 LP) and a stabilized blue LED (470 nm) were used. Images were acquired with an EM-CCD camera (Hamamatsu ImagEM X1) set to 20 ms exposure time at an acquisition rate of 50 Hz and 200 x EM gain. LED power was set in each experiment to yield good photon count and acceptable signal-to-noise ratio (typically: 0.07–0.09). A general iGluSnFR experiment contained of 10-20 imaging trials for homoeostatic plasticity experiments and 20-40 trials for all other experiments. For each trial 30 frames were recorded. During each trial the neurons were stimulated once at frame 20 via field potential to elicit one AP per trial, which eventually results in synaptic release. Trials were repeated every 20 s.

## QUANTIFICATION AND STATISTICAL ANALYSIS

### dSTORM nanocluster analysis

Density histogram images from the Leica image acquisition software (LAS X Life Science, Leica Microsystems) were imported to ImageJ (Schindelin, J., Arganda-Carreras, I., Frise, E. et al., 2012) for subsequent cluster analysis of RIM1 localizations. Images were segmented according to grayscale pixel values with lower thresholds for RIM1 = 20 to define clustered molecules. Only localizations larger than 800 $nm^2$ were defined as nanoclusters and included in the cluster analysis. Nanoclusters smaller than 800 $nm^2$ represent non-clustered molecules. To define synaptic areas, the Synapsin I laser widefield images were also segmented according to pixel grayscale values. Here, the lower threshold was calculated as 20% of the maximum grayscale intensity in each individual image (see Figure S4: Cluster analysis). The generated Synapsin I ROIs were then superimposed on the individual RIM1 density histograms to define synaptic and extrasynaptic nanoclusters. Nanoclusters that were completely superimposed on Synapsin I were defined as synaptic while nanoclusters without any overlap with Synapsin I were defined as extrasynaptic. Gray values of RIM1 localizations were measured in the previously defined nanoclusters, which correspond to the number of molecule localizations inside the nanoclusters. To investigate the number of non-clustered RIM1 molecules, the GFP widefield image was used to segment and define the axon. All RIM1 molecule localizations in the rendered image, independently of the size within the axon were quantified. Local background measurements were used to subtract the background. The number of non-clustered molecules was calculated by subtracting the number of clustered RIM1 localizations from the number of all RIM1 molecule localizations. In the control 57% (±4.4%) of RIM1 molecules were non-clustered, while 68% (±4.1%) for shSRPK2 and 54% (±2.4%) for SRPK2 overexpression. The generation of density maps was done using custom-written algorithms in Mathematica 11 (Wolfram) with a defined radius of 15 nm.

### Electron microscopy

3D image stacks were aligned with StackReg Plugin in ImageJ (P. Thévenaz, U.E. Ruttimann, M. Unser, A Pyramid Approach to Subpixel Registration Based on Intensity, IEEE Transactions on Image Processing, vol. 7, no. 1, pp. 27-41, January 1998) and synapses were rendered with Imaris 9.1.0. Docked vesicles from random synapses were manually identified and counted with help of EspINA Software (EspINA Interactive Neuron Analyzer). The postsynaptic density (PSD) area was calculated by multiplying PSD length by slice thickness and summing these values of all PSD containing slices with MatLab (MatLab, R2015b)

### Analysis of FM4-64 styryl dye imaging experiments

Image series were analyzed with ImageJ 1.51 and Igor Pro 7.0 Software. Image stacks were registered with StackReg Plugin in ImageJ. Even before stimulation there is a slow loss of fluorescence from synapses which is caused by spontaneous vesicle release and photo-bleaching. To separate the two processes, and be able to correct our measurements of dye fluorescence over time for

bleaching, we measured spontaneous release in isolation by strongly reducing excitation light intensity which avoids photobleaching. Total bleaching over the entire imaging period amounted to only ~2% and occurred in an exponential fashion with a tau of 7,800 frames. For each image series, we defined 40-80 regions of interests (based on circular shape, center of mass and 1-2 μm diameter) and average fluorescence intensity was measured per region of interest. These average intensity values were background corrected by subtracting the weak fluorescence remaining after the final rounds of high-frequency stimulation (see above). Bleaching-correction was performed with the estimated time course of photo-bleaching. Corrected intensity values for each ROI in an experiment were fit to the sum of two exponential decay functions to extract the time constant of fluorescence loss due to electrical stimulation ($\tau_e$).

The fitting function assumes that spontaneous and evoked vesicle release are drawn from distinct pools and happen independently. The first exponential term represents the spontaneous release happening throughout the entire experiment. The second exponential term describes evoked release starting with onset of stimulation. We extract $A_{sp}$ and $A_e$, which denote the amplitudes of the spontaneous and evoked component of release, respectively. Furthermore, we report the inverse of $\tau_e$ as the evoked release rate ($1/\tau_e$), a parameter being proportional to the release probability. The evoked release rates of individual ROIs per experiment are log-normal distributed. Therefore, we calculated the geometric mean per experiment and averaged the geometric means per condition for statistical comparison.

### Analysis of iGluSnFR experiments

Image analysis was performed with Image J and Igor Pro 7.0 Software. Multiple image stacks of different trials within one experiment were registered to the first image of the first trial with StackReg Pro Plugin for ImageJ. To identify release sites, for each trial a response image was calculated by subtraction of the baseline (average of four images just before stimulation) from the response (average of two images after stimulation). Response images were filtered with a Gaussian blur filter (three pixel) and then projected for maximum intensity. Release sites were detected with auto local threshold method "phansalkar" in ImageJ. For detected particles a ROI set was generated and for the analysis only ROIs with a rounded shape were selected. Multi-synaptic ROIs, i.e. ROIs with release from more than one synapse, identified by center of gravities that were more than 500 nm apart in different trials, were discarded (cf Figure S1E).

For the ROIs that were preselected by this approach ΔF/F traces in each trial were calculated by subtraction of the baseline fluorescence from the fluorescence at each time point, divided by the baseline fluorescence. For the final analysis, only ROIs that had at least one clear response after stimulation during any trial (i.e. a peak ΔF/F larger than 4x standard deviation of the baseline noise, cf Figure S1F) and low baseline noise (standard deviation smaller than 0.045, Figure S1G) were considered.

For each ROI ΔF/F traces were calculated for each trial based on the mean fluorescence of the ROI. 10-20 and 20-40 of such traces for homoeostatic plasticity experiments and all other experiments, respectively, were averaged and the peak ΔF/F amplitude from this average trace was determined for that synaptic structure/ROI. This peak ΔF/F value was then averaged across all synaptic structures of one culture/experiment. To illustrate the mean response of a certain condition the mean trial ΔF/F traces were averaged across all synaptic structures/ROIs within a culture/experiment.

To verify that the overexpression of SRPK2 lead to an increase of the release sites N, while the vesicular release probably $p_{ves}$ is unaltered, we applied variance-to-mean ratio (VMR) and $1/CV^2$ analysis as described in (Huijstee and Kessels, 2020) to the ΔF/F iGluSnFR peak amplitudes in our experiments. For ROIs that passed the selection criteria, the ΔF/F time course of each trial was fitted to an iGluSnFR response template to determine the peak amplitude. The fitted ΔF/F amplitudes were not allowed to be negative, so that the minimum ΔF/F peak value was set to 0. The measured amplitudes were run-down corrected and the corrected amplitudes from the different trials were used to calculate the VMR and $1/CV^2$ for each ROI.

### FLIM analysis

Fluorescence intensity decay curves of mNeon in presence and absence of mRFP were imported in Igor Pro and global double exponential fitting was performed using the following formula:

$$F(t) = a_1 e^{-(t-t_0)/\tau_1} + a_2 e^{-(t-t_0)/\tau_D} + y_0$$

where $a_i$ is amplitude (constrained between 0 and 5), $\tau_1$ is a fast lifetime component (constrained between 0 and 3.3 ns), $\tau_D$ is a slow decay component (fixed at the value of mNeon-C2A/B alone, which is 3.2 ns), $x_0$ and $y_0$ are offsets. $\tau_1$ was linked across all experiments.

Resulting $a_1$ values (interaction fractions) were plotted against SRPK2-mRFP concentration and fitted globally using the Hill function:

$$F(x) = min + \frac{\max - min}{1 + \left(K_D / x\right)^n}$$

where min is fixed to 0, max is linked across all experiments and constrained between 0 and 100%, n (stoichiometry) is linked, $K_D$ is dissociation constant.

### Processing of maxquant data

MaxQuant outputs were further processed using phosphoprocessR version 0.99.8 (available as R package on github here: https://github.com/awaardenberg/phosphoProcessR), in R version 3.5.1 (Gentleman et al., 2004), which implements methods previously described (Engholm-Keller et al., 2019; Waardenberg, 2017), with the following differences. Phosphopeptides were remapped to the same fasta file used for MaxQuant quantification (see above) and centered peptide sequences with a window of +/− 7AA around each phosphorylated site annotated. Phosphopeptides were retained if a site localization score $\geq$ 0.75 (class I) for at least one site within a phosphopeptide for one experiment (where an experiment was an intensity reading from a TMT label), was observed. For multi-phosphorylated peptides, all additional sites belonging to the peptide with a class I site must have had a score greater than 0.5. Where multiple measurements were obtained for the same phosphopeptide, the median log2 transformed intensity of all measurements were used. Measurements that mapped to more than one unique protein identifier were assigned a unique multi-mapped identifier. For SRPK2 phosphoproteome data, only complete data (no missing values for any replicates) was used (without imputation), followed by quantile normalization (Dudoit et al., 2002) and surrogate variable analysis (Leek and Storey, 2007), with a prior model describing three groups – SRPK2, shSRPK2 and control. Principle component analysis and hierarchical clustering was used for guiding the impact of correction. For differential phosphorylation analysis of SRPK2 data, we fit a generalized linear model with Bayes shrinkage as implemented in limma version 3.36.5 (https://bioconductor.org/packages/release/bioc/html/limma.html) (Ritchie et al., 2015) and compared shSRPK2 vs. Ctrl and SRPK2 vs. Ctrl together (total complete data) and individually (as independent datasets). Where analyzed independently, normalization and surrogate variable analysis were applied to only the conditions compared. All p values reported for SRPK2/shSRPK2 vs the control were first calculated as a moderated t test and then corrected for multi-hypothesis testing using the Benjamini and Hochberg (FDR) method (Benjamini and Hochberg, 1995). All data are available in Tables S1, S2, and S3. The mass spectrometry proteomics data have been deposited to the ProteomeXchange Consortium via the PRIDE partner repository with the dataset identifier PXD016636.

For classification of RIM1 *in vitro* phosphorylation sites, MaxQuant data were remapped using phosphoprocessR without imputation or surrogate variable analysis and converted to a boolean, present or absent call, based on detection in RIM1 or control replicates. A one-tailed Fishers exact test was used to test for increased detection relative to control, specifically for RIM1 sites (Fisher, 1956).

### Protein kinase substrate prediction

Protein kinase substrate prediction was performed using the first stage only of protein kinase activity prediction provide by KinSwingR version 1.1.4 (available on R/BioConductor here: http://bioconductor.org/packages/KinSwingR/). In brief, each kinase, K, is modeled as a position weight matrix, $PWM_{a,p}$, representing the log likelihood ratio of the average frequency of amino acid residue, $a$, at each position, $p$, divided by background frequencies, $B$ ($C$ is a pseudo count to avoid log zero and $B$ is fixed to 0.05) (Equation 1).

$$PWM_{a,p} = \log\left(\frac{\left(\frac{1}{n}\sum_{i=1}^{n} K_i\right) + C}{B_a + C}\right) \quad \text{(Equation 1)}$$

### SRPK2 motif

SRPK2 motifs were generated from annotated and *in vitro* data for RIM1. Motif position weight matrices were built from inputting sequencing into the viewPWM function of KinSwingR. Previously published SRPK2 targets were used to generate a SRPK2 motif (Table S3, Daub et al., 2002; Duarte et al., 2013; Hong et al., 2012; Jang et al., 2008; Wang et al., 2017). For *in vitro* data, all RIM1 sites with an FDR <0.2 were retained for building a SRPK2 motif, utilizing the buildPWM function in KinSwingR, with either "S" or "S/T" centered phosphorylation site peptides. The information content at each position (described as bits) of each PWM, was modeled as per Equation 2 and visualized as a Shannon Entropy model (Schneider and Stephens, 1990), where bits of each position, $bits_p$, are described as the difference between the maximum information content, where n = 20 (number of amino acids) and uncertainty at each position, $p$, for amino acid, $a$.

$$bits_p = log_2(n) - \left(\sum_{a=a}^{t} f(a,p) log_2 f(a,p)\right) \quad \text{(Equation 2)}$$

Groups of amino acids are colored according to the Shapely scheme, where each AA has a unique color and polar/non-polar AAs are brighter/dull.

### *In silico* RIM1 – SRPK profile

For each serine "S" or threonine "T" amino acird (AA) along the length of the RIM1 "Q9JIR4_SS" Rat protein sequence, a custom R script was used to *in silico* digest and obtain centered "S/T" sequences +/− 7AA. A random background was generated separately for "S" and "T" *in silico* digested peptides, whereby non-centered surrounding AAs were drawn randomly with replacement from all

20 AAs and 1000 random peptides centered on an "S" or "T". The set of in-silico peptides and random background were input into the scoreSequences function of KinSwingR to test for matching of kinase PWMs against each centered peptide sequence. Resulting scores, $S_{score}$, are as described above and probabilities are corrected using the Benjamini and Hochberg (FDR) method (Benjamini and Hochberg, 1995).

### Statistical analysis of data

Data are shown as mean ± standard errors of the mean (SEM) throughout the study. One-Way ANOVA with Holm-Sidak correction for multiple comparisons was performed for statistical analysis of experiments with more than two conditions. t-tests were used to compare two conditions if not stated differently. We found the amplitudes of stimulated iGluSnFR responses to be log-normally distributed and therefore performed statistical tests on log-transformed amplitude values. All tests were two-sided and differences were considered statistically significant if $p < 0.05$. Significant differences are indicated in the figures by an asterisk (*). Statistical analyses were performed with Prism GraphPad (Version 6.02).